HHS Public Access

Author manuscript

Nature. Author manuscript; available in PMC 2021 April 19.

Published in final edited form as:

Nature. 2018 June ; 558(7711): 553–558. doi:10.1038/s41586-018-0215-y.

Cryo-EM structure of human rhodopsin bound to an inhibitory G protein

Yanyong Kang[1,12], **Oleg Kuybeda**[2,12], **Parker W. de Waal**[1,12], **Somnath Mukherjee**[3], **Ned Van Eps**[4], **Przemyslaw Dutka**[3,5], **X. Edward Zhou**[1], **Alberto Bartesaghi**[2], **Satchal Erramilli**[3], **Takefumi Morizumi**[4], **Xin Gu**[1], **Yanting Yin**[1], **Ping Liu**[6,7], **Yi Jiang**[7], **Xing Meng**[8], **Gongpu Zhao**[8], **Karsten Melcher**[1], **Oliver P. Ernst**[4,9], **Anthony A. Kossiakoff**[3,10,*], **Sriram Subramaniam**[2,11,*], **H. Eric Xu**[1,7,*]

[1]Center for Cancer and Cell Biology, Innovation and Integration Program, Van Andel Research Institute, Grand Rapids, MI, USA. [2]Cancer Research Technology Program, Frederick National Laboratory for Cancer Research, Frederick, MD, USA. [3]Department of Biochemistry and Molecular Biology, University of Chicago, Chicago, Illinois, USA. [4]Department of Biochemistry, University of Toronto, Toronto, Ontario, Canada. [5]Faculty of Biochemistry, Biophysics and Biotechnology, Jagiellonian University, Krakow, Poland. [6]University of Chinese Academy of Sciences, Beijing, China. [7]Key Laboratory of Receptor Research, VARI-SIMM Center, Center for Structure and Function of Drug Targets, Shanghai Institute of Materia Medica, Chinese Academy of Sciences, Shanghai, China. [8]David Van Andel Advanced Cryo-Electron Microscopy Suite, Van Andel Research Institute, Grand Rapids, MI, USA. [9]Department of Molecular Genetics, University of Toronto, Toronto, Ontario, Canada. [10]Institute for Biophysical Dynamics, University of Chicago, Chicago, IL, USA. [11]Center for Cancer Research, National Cancer Institute, NIH, Bethesda, MD, USA. [12]These authors contributed equally: Yanyong Kang, Oleg Kuybeda, Parker W. de Waal.

Abstract

G-protein-coupled receptors comprise the largest family of mammalian transmembrane receptors. They mediate numerous cellular pathways by coupling with downstream signalling transducers, including the hetrotrimeric G proteins G_s (stimulatory) and G_i (inhibitory) and several arrestin proteins. The structural mechanisms that define how G-protein-coupled receptors selectively couple to a specific type of G protein or arrestin remain unknown. Here, using cryo-electron microscopy, we show that the major interactions between activated rhodopsin and G_i are mediated by the C-terminal helix of the G_i α-subunit, which is wedged into the cytoplasmic cavity of the

[*]**Correspondence and requests for materials** should be addressed to A.A.K., S.S. or H.E.X., koss@bsd.uchicago.edu; ss1@nih.gov; eric.xu@vai.org.

Author contributions Y.K. initiated the project, prepared samples, performed data acquisition and structure determination, and prepared the figures and manuscript writing; H.E.X. and K.M. conceived the project and designed the research, and wrote the paper with contributions from all authors; O.K., X.E.Z., A.B. and S.S. performed image processing, structure determination, figure preparation, and manuscript writing; P.W.d.W. performed computational experiments, analysed the structure, prepared figures, and manuscript writing; P.D., S.M., S.E. and A.A.K. designed and performed Fab selection; N.V.E., T.M. and O.P.E. designed and performed DEER experiments; X.G., Y.Y., P.L. and Y.J. performed cell-based assays; G.Z. and X.M. helped with data collection.

Competing interests The authors declare no competing interests.

Extended data is available for this paper at https://doi.org/10.1038/s41586-018-0215-y.

Supplementary information is available for this paper at https://doi.org/10.1038/s41586-018-0215-y.

transmembrane helix bundle and directly contacts the amino terminus of helix 8 of rhodopsin. Structural comparisons of inactive, G_i-bound and arrestin-bound forms of rhodopsin with inactive and G_s-bound forms of the β_2-adrenergic receptor provide a foundation to understand the unique structural signatures that are associated with the recognition of G_s, G_i and arrestin by activated G-protein-coupled receptors.

The selective coupling of cell-surface receptors with specific intracellular effector proteins is a fundamental step in transmembrane signalling. G-protein-coupled receptors (GPCRs) constitute the largest protein family of transmembrane receptors with more than 800 members in humans[1]. These receptors signal primarily through intracellular G proteins and arrestin proteins. Compared to the vast diversity of the GPCR family members and their physiological functions, the number of intracellular signalling transducers are much limited, with only four major types of G protein[2] (Fig. 1a) and two major types of arrestin[3]. These distinct signalling transducers regulate the generation of a variety of secondary messengers and activate various downstream kinases, which lead to diverse cellular signalling pathways and physiological consequences. Thus, the selective coupling of a specific transducer protein by a GPCR is crucial for cellular signalling and responses to extracellular stimuli.

Our understanding of GPCR signalling has been greatly enhanced by the remarkable progress in GPCR structural biology, including the determination of over 170 structures from 40 unique GPCR members in active or inactive states and in complex with G_s or arrestin[4]. In the inactive states, the cytoplasmic end of the seven-transmembrane-helix domain (TMD) is closed[5–7], thus preventing GPCRs from effective coupling with cellular signalling transducers. Agonist binding induces conformational changes in the TMD, including an outward movement at the cytoplasmic end of transmembrane helix 6 (TM6)[8–13], which opens a cavity in the TMD bundle for interaction with one or more specific transducer proteins. This mechanism is particularly highlighted by the notable outward movement (14–18 Å) at the cytoplasmic side of TM6 in the G_s-bound β_2-adrenergic receptor (β_2AR) structure[14] and the recent cryo-electron microscopy (cryo-EM) structures of G_s-bound class B GPCRs[15,16]. Combination of the structural observations with sequence analyses has revealed a barcode system in G proteins for GPCR–G-protein binding selectivity[17]. However, less is known about the mechanisms determining selectivity on the receptor, in particular the subset of G_i-coupled receptors, despite the fact that they constitute the largest fraction of GPCR proteins[17].

Rhodopsin is a prototypical GPCR that plays a crucial role in light perception and has served as a model system for studying GPCR signalling[18–20]. In the pre-illuminated state, rhodopsin adopts an inactive conformation stabilized by the inverse agonist, 11-*cis*-retinal. Light induces isomerization of the retinal ligand to the all-*trans*-retinal (ATR) configuration, which activates the receptor. The activated rhodopsin is coupled to the G protein transducin (G_t) (Fig. 1a), which is a G_i homologue[21,22], to initiate the light-sensing signalling pathways. To understand the structural basis for the selective coupling of G_i by a GPCR, we determined the structure of the rhodopsin–G_i complex at a near atomic resolution using cryo-EM.

Cryo-EM of the rhodopsin–G_i complex

To prepare a stable rhodopsin–G_i complex for structural studies, we took advantage of a constitutively active form of rhodopsin (termed 4 M, containing mutations $N2^{Nterm}C$, $E113^{3.28}Q$, $M257^{6.40}Y$, $N282^{ECL3}C$; superscripts denote Ballesteros–Weinstein numbering), that was previously used to determine the structure of the rhodopsin–arrestin complex[23,24]. In cell-based assays, the constitutively active rhodopsin activates the G_i coupling pathway more strongly than the wild-type receptor (Fig. 1b). Importantly, wild-type and constitutively active rhodopsin do not activate the G_s pathway regardless of the presence of ATR (Extended Data Fig. 1c). Because previous studies indicated that the active rhodopsin–G_i complex is more stable than the active rhodopsin–G_t complex[25], we focused on obtaining a stable complex of activated rhodopsin bound to a dominant-negative mutant form of G_i (Extended Data Fig. 1a, b), which was used to promote the nucleotide-free form of G_i[26]. To further stabilize the rhodopsin–G_i complex, we screened a panel of antibodies against the dominant-negative G_i from a phage display Fab library by negative-stain electron microscopy to identify one Fab fragment, termed Fab_G50, which stabilized the rhodopsin–G_i complex. The conformational state of rhodopsin in complex with G_i and Fab was surveyed by high-resolution distance mapping with site-directed spin labelling and double electron–electron resonance (DEER) spectroscopy in detergent micelles (Fig. 1c and Extended Data Fig. 1d–f). Almost identical distances were measured when rhodopsin was bound to G_i in the presence or absence of Fab_G50, suggesting that the Fab fragment does not affect the conformation of rhodopsin. In addition, the distance distributions of TM6 and TM7 relative to TM2 are nearly identical between G_i-bound and G_t-bound rhodopsin[27,28] (Extended Data Fig. 1e).

The cryo-EM structure of the rhodopsin–G_i–Fab complex was determined at a nominal global resolution of 4.5 Å (Fig. 1d and Extended Data Fig. 2a–f), which reveals a well-defined density map for the rhodopsin seven-transmembrane bundle, the $G\alpha_i$ Ras-like domain, and the Gβ and Gγ subunits (Fig. 2a, b and Extended Data Fig. 3a–g). The position of the α-helical domain (AHD) of $G\alpha_i$ is well defined owing to the direct stabilization of this domain by the Fab fragment, which simultaneously interacts with the $G\alpha_i$ AHD and the Gβ subunit (Fig. 1d). The binding site of the Fab fragment is far away from the rhodopsin–G_i interface, consistent with the fact that Fab binding did not affect the conformation of rhodopsin.

The rhodopsin–G_i interface

The structure of the rhodopsin–G_i complex (Fig. 2a, b and Extended Data Table 1) reveals that interactions between rhodopsin and G_i are exclusively mediated through the $G\alpha_i$ subunit, and that there is no contact between rhodopsin and the Gβγ subunits. The most important interface between rhodopsin and $G\alpha_i$ is formed by the last 11 residues of the C-terminal α5-helix of $G\alpha_i$ (Fig. 2c, d), consistent with its known crucial role in receptor binding[29–35]. In the complex, the C-terminal 11 residues (residues 344–354) of $G\alpha_i$ adopt a straight amphipathic helix (α5-helix) to residue C351, followed by a three-residue loop (residue 352-GLF-354) (Fig. 3a, b).

The negatively charged dipole of the C terminus of the α5-helix forms an electrostatic interaction with the positively charged dipole of the N terminus of helix 8 of rhodopsin, with the carbonyl group of G352 forming the capping interaction with the N-terminal amine groups of helix 8 of rhodopsin (Fig. 3c). The cytoplasmic side of the rhodopsin transmembrane bundle is highly positively charged and this is known to be a common feature of GPCR structures[23]. Sequence alignment of all $G\alpha_i$ and $G\alpha_t$ subtypes reveals a conserved sequence pattern (Fig. 3d), including D350 and G352, which is at the terminus of the α5-helix and allows the uncapped carbonyl group of α5-helix to form charge interactions with helix 8 of rhodopsin (Fig. 3b). The G352C-mutated $G\alpha_i$ did not crosslink with rhodopsin with cysteine mutations around the transmembrane bundle (Extended Data Fig. 4a, b), consistent with the finding that the G352C mutation in G_i disrupts its binding capability to rhodopsin.

Beside the charge interactions, the two large hydrophobic side chains L353 and L348 are directed towards the hydrophobic pocket of rhodopsin formed by TM3, TM5, TM6 and TM7 (Fig. 3a, b). Replacement of these two residues by alanine, together with G352A, has marked effects on G_i binding to rhodopsin[36]. Residues I344, K345 and C351 of $G\alpha_i$ are also within packing distance with TM3, TM5 and TM6 (Fig. 3a, b), and alanine mutations in these residues also show reduced G_i binding to rhodopsin[36]. Thus, our structural studies provide a structural explanation to rationalize the extensive mutagenesis studies on the effect of the last 11 residues of the C terminus of $G\alpha_i$[36].

The second and less extensive interface between rhodopsin and G_i is mediated through the N-terminal helix (αN-helix) of $G\alpha_i$, where its residues (E28 and R32) are in proximity to interact with the intracellular loop (ICL2) between TM3 and TM4 (Extended Data Fig. 5c). In contrast to a short α-helix formed by the ICL2 loop in the arrestin-bound rhodopsin structure[23], ICL2 in the G_i-bound complex adopts an extended loop. The presence of the interface between ICL2 and αN-helix was confirmed by site-specific disulfide crosslinking from cysteine mutations in residue E28 in $G\alpha_i$ to residues $N145^{ICL2}$ and $F146^{ICL2}$ in ICL2 of rhodopsin (Extended Data Fig. 4c, d), in agreement with previous crosslinking results between $G\alpha_t$ and light-activated rhodopsin by a chemically activated crosslinking reagent[37]. Furthermore, R32A in $G\alpha_i$ is a rare mutation that increases the binding of $G\alpha_i$ to rhodopsin[36]. On the basis of the structure, the large side chain of R32 in $G\alpha_i$ is in the position that could interfere with the close interactions between the αN-helix in $G\alpha_i$ and the ICL2 of rhodopsin and the removal of the large side chain in R32A mutations could thus enhance rhodopsin–Gi interactions.

Crystal structures of rhodopsin have been determined in several different states, including the inactive/inverse agonist-bound state[5] and the active arrestin-bound or GαCT-bound state[10,12] (GαCT is a high-affinity peptide from the C terminus of $G\alpha_t$). Comparisons of these structures reveal intriguing conformational differences in rhodopsin between each state (Fig. 4a). Compared to the inactive state, the G_i-bound rhodopsin structure has an extended TM5 and outward movements in TM6, TM1 and TM4 at the cytoplasmic side (Fig. 4a, Supplementary Video 1), which results in an elastic pocket for binding the G protein. The overall structure of rhodopsin bound to G_i is similar to that bound to the GαCT, consistent with the equivalence of rhodopsin coupling with G_i and G_t (Fig. 4b). The conformation of

the C-terminal 11 residues overlaps well with the structure of GαCT. However, the position of the GαCT is shifted a half-helical turn (approximately 2.2 Å) deeper into the rhodopsin helical bundle owing to the lack of constrain on the GαCT peptide (Fig. 4b).

Structural comparison of rhodopsin in the G_i-bound and arrestin-bound states also reveals notable differences in the receptor conformation, including TM1, TM4, TM6 and helix 8 (Fig. 4a, Supplementary Video 2), as well as ICL2, which adopts a short α-helix in arrestin-bound rhodopsin but exists as an extended loop in the G_i-bound state (Fig. 4a). These conformational differences may represent the unique structural signatures of rhodopsin to distinguish between G protein and arrestin. In addition, other factors such as phosphorylation at the rhodopsin C-terminal tail may further enhance the specific interactions of arrestin with the activated receptor[24].

Structural basis of G_i and G_s selectivity

Rhodopsin and β_2AR are the two best studied GPCRs that are coupled to G_i and G_s, respectively. Structural comparisons between these two receptors reveal the basis for selective coupling of G_i and G_s by a GPCR. In the inactive state, both receptors adopt a very similar closed conformation, in which the cytoplasmic ends of TM6, TM1, TM2, TM4 and the turn between TM7 and helix 8 are in nearly identical positions to each other (Fig. 5a, b). In the active state, the cytoplasmic ends of TM2 and TM4 of both receptors remain in identical position, but the cytoplasmic ends of TM6, TM1 and the turn between TM7 and helix 8 differ considerably between the two receptors (Fig. 5c, d, Supplementary Video 3). In particular, the cytoplasmic end of TM6 in rhodopsin is shifted inward by approximately 8 Å relative to that of TM6 seen in the G_s-bound β_2AR complex or in the G_s-bound class B GPCR structures (Extended Data Fig. 5a–d). Correspondingly, the α5-helix of $G\alpha_i$ is rotated 20° away from TM6 towards helix 8 and forms a capping interaction with the N-terminal dipole of helix 8 (Fig. 3a, b). Compared to the straight α5-helix in $G\alpha_i$, the α5-helix in $G\alpha_s$ is slightly kinked (Fig. 5d), which allows the C terminus of this helix to orient away from helix 8 towards TM6 of rhodopsin. Accompanying the 20° rotation of the α5-helix between $G\alpha_i$ and $G\alpha_s$ is a rigid body rotation of the G_i heterotrimer, which displays rearrangements up to 16 Å in the areas of the $G\alpha_i$ N-terminal end and Gγ subunits (Fig. 5e, f). The observed differences between binding of G_i and G_s to their receptors are in good agreement with a model of the rhodopsin–Gi complex that resulted from experimental DEER distance mapping[28]. On the basis of these structural observations, we reason that the conformational difference in the TM6 between rhodopsin and β_2AR is one of the major determinants for the coupling specificity of G_i and G_s in the two receptors. This movement of TM6 upon activation is a general theme in seven-helix transmembrane receptors, and was originally observed in cryo-EM studies of light-induced conformational changes in the proton pump bacteriorhodopsin[38,39].

An additional cause of the coupling specificity of G_i and G_s between rhodopsin and β_2AR may reside in the regions of the TM5–α4-helix interface (Extended Data Fig. 5e, f). Superposition of G_s and G_i in the two receptor complexes reveals a steric collision between the extended TM5 of β_2AR and α4-helix of $G\alpha_i$, consistent with the involvement of this region in receptor coupling specificity[40,41].

Structural comparison of our nucleotide-free G_i complex with the GDP-bound inactive G_i complex also reveals an interesting mechanism of rhodopsin-mediated G_i activation (Extended Data Fig. 6a). Upon binding to rhodopsin, the α5-helix was rotated by 90° and extended by two additional helical turns into the rhodopsin cytoplasmic pocket (Extended Data Fig. 6b), which resulted in conformational changes in the loop between β6 and α5-helix, a key structural element of the GDP-binding pocket. This conformational change leads to a movement of α1-helix into the GDP-binding pocket, thus expelling the GDP from its pocket (Extended Data Fig. 6c, d). The release of GDP from $G\alpha_i$ induces separation of the $G\alpha_i$ Ras domain from its AHD, the conformation of which was captured by the Fab fragment as observed in our structure. The mechanism of rhodopsin-mediated G_i activation is similar to that of β_2AR-mediated G_s activation[14,42,43], suggesting a common mechanism of GPCR-mediated G protein activation.

To gain further insight into differential conformational dynamics of TM6 between active rhodopsin and β_2AR, we performed all-atom mollified adaptive biasing potential (mABP) simulations of the receptors with the fABMACS software package to accelerate sampling[44] (Extended Data Table 2). By calculating the free energy landscape of TM6 movement relative to the receptor transmembrane bundle (Extended Data Fig. 7a, b), these biased simulations revealed that the dynamic range of TM6 of rhodopsin is considerably less than that of β_2AR (Fig. 6a–c). Furthermore, the TM6 of rhodopsin was unable to swing outwards to sample conformations comparable to that of β_2AR, resulting in steric clashes between rhodopsin TM6 and G_s, consistent with the inability of rhodopsin to couple with G_s (Fig. 6c and Extended Data Fig. 1b). To extend this mechanism to other class A GPCRs, we performed similar simulations for the μ-opioid receptor 1 (μOR1)[45], a G_i-coupled receptor, and the adenosine A_{2A} receptor (A_{2A}R)[20], a G_s-coupled receptor. These simulations also revealed that TM6 of μOR1 remained in a more closed conformation, whereas TM6 of A_{2A}R favoured an outward conformation (Fig. 6a–c and Extended Data Fig. 7c, d). We note however that both G_s coupler simulations were performed in the absence of a complete ICL3, whereas both G_i couplers had their ICL3 intact. Additional simulations with ICL3-truncated G_i couplers revealed no notable differences compared to the full-length receptor (Fig. 6b), indicating that their ICL3 was not sufficient to restrict the outward movement of TM6. Together, these results suggest that conformational differences in TM6 may represent the basis for stratification of GPCRs into distinct conformational groups with respect to the coupling specificity for G_i or G_s by GPCRs[46] (Fig. 6d).

TM6 sequence motif for G_i selectivity

To investigate the basis for the different TM6 dynamics between G_i and G_s coupling GPCRs, we performed sequence analysis on TM6, which reveals that G_i- and G_s-coupled receptors exhibit distinct, inversely related enrichment patterns for polar and hydrophobic residues at the membrane interface (Extended Data Fig. 8a–c). For G_i-coupled receptors, an enrichment of polar, often positively charged, residues at TM6.31/34/35 could act to stabilize the receptor within the charged lipid head groups thus preventing outward movement of TM6 (Extended Data Fig. 8c). By contrast, an enrichment of hydrophobic residues found in G_s coupling receptors would promote an outward swing of TM6 favouring interactions with the hydrophobic lipid tails. In addition, we found another potential selectivity filter at TM6.36

where G_i and G_s couplers exhibit differential enrichment of polar/hydrophobic residues. Comparison of our G_i-bound rhodopsin to G_s-bound β_2AR and miniG_s-bound A_{2A}R shows that M253$^{6.36}$ of rhodopsin forms a hydrophobic interaction with L353 of Gα_i, whereas T274$^{6.36}$ of β_2AR and S234$^{6.36}$ of A_{2A}R do not appear to interact with the G_s or miniG_s (Extended Data Fig. 8d–f). Instead these polar residues in G_s-coupled receptors are enriched near an extra kink specifically in the TM6 helix of G_s-coupled receptors. We questioned whether they may have a role to destabilize TM6 and promote its outward kink. Indeed, throughout simulations, both S234 and T274 form extensive hydrogen bonding with the kinked TM6 backbone of β_2AR and A_{2A}R (Extended Data Fig. 8g). We speculate that the polar/non-polar residue distribution in TM6 may contribute to differential conformational dynamics of TM6 between G_i- and G_s-coupled receptors.

In summary, our results show that the conformational change, especially the outward movement of TM6, is less pronounced for G_i-bound rhodopsin than the corresponding movement in the G_s-bound β_2AR structure. This conformational difference seems to be the key determinant for the different docking of the C-terminal α5-helix between Gα_i and Gα_s into the receptor transmembrane bundle. Energy landscape analysis of a different set of G_i- and G_s-coupled receptors also revealed that they have similar profiles to those of rhodopsin and β_2AR, respectively, with respect to the position of TM6. Sequence analysis reveals that the differential swing of TM6 between G_i- and G_s-coupled receptors could be attributed to different polar/nonpolar residue distribution in the TM6. Together, these data suggest that the basis for G_i- and G_s-coupling selectivity observed in rhodopsin and β_2AR is a general theme for GPCRs to distinguish between G_i and G_s receptors. G_i-coupled receptors represent the largest subgroup of receptors in the GPCR superfamily. On the basis of the common features of the positively charged transmembrane bundle of GPCRs and the conserved sequences of the α5-helix in Gα_i, we expect that the structure of the rhodopsin–G_i complex will serve as a model for understanding signalling of other G_i-coupled receptors.

Online content

Any Methods, including any statements of data availability and Nature Research reporting summaries, along with any additional references and Source Data files, are available in the online version of the paper at https://doi.org/10.1038/s41586-018-0215-y.

METHODS

No statistical methods were used to predetermine sample size. The experiments were not randomized, and investigators were not blinded to allocation during experiments and outcome assessment.

Constructs and expression of human rhodopsin.

Human rhodopsin with four mutations, N2^{Nterm}C, E113$^{3.28}$Q, M257$^{6.40}$Y and N282^{ECL3}C, was cloned into pFastBac vector. To facilitate expression and purification, an N-terminal 8× His-sfGFP-BRIL epitope and a TEV protease site were inserted after sfGFP. These constructs were expressed in Sf9 insect cells using the Bac-to-Bac Baculovirus system (Invitrogen). The cells were infected with baculovirus at 27 °C for 48 h before collection.

Constructs, expression and purification of G_i heterotrimer.

The heterotrimeirc G_i complex was expressed in Sf9 insect cells (Invitrogen). Human $G\alpha_i$ was cloned in pFastbac vector with 6× His-MBP at the N terminus, and the virus was prepared using Bac-to-Bac system (Invitrogen). Rat Gβ1 and N-terminal 6× His-MBP tagged bovine $G\gamma_2$ were cloned into a pFastBac vector. The virus was prepared using the Bac-to-Bac system. The cells were infected with both $G\alpha_i$ and $G\beta\gamma$ virus at 27 °C for 48 h before collection, and the ratio was determined by small-scale titration experiment. The G_i heterotrimer was purified as previously described[26].

DEER spectroscopy.

Generation of rhodopsin mutants, expression in HEK293S GnTI$^-$ cells, and spin-labelling with 1-oxyl-2,2,5,5-tetramethyl-Δ^3-pyrroline-3-methyl) Methanethiosulfonate (MTSSL, Toronto Research Chemicals) was as previously described[47]. For DEER measurements, spin-labelled rhodopsin mutants bound to a 1D4-antibody (MA1–722, ThermoFisher)-conjugated column were thoroughly washed and complexed with G_i heterotrimer or with the G_i-Fab_G50 complex in 20 mM HEPES, pH 7.2, 100 mM NaCl, 0.02% *n*-dodecyl-β-D-maltopyranoside (DDM), 0.004% cholesteryl hemisuccinate (CHS) and 5 μM ATR under yellow (>500 nm) light illumination on ice. The entire rhodopsin–G_i or rhodopsin–Gi–Fab_G50 complex was then further washed and eluted from the 1D4 column with 20 mM HEPES, pH 7.2, 100 mM NaCl, 0.1% digitonin, 150 μM 1D4 peptide and 5 μM ATR. The eluate was concentrated, and 20% (v/v) deuterated glycerol was added. The complexes were added to quartz capillaries (1.5 mm inner diameter and 1.8 mm outer diameter) and flash-frozen using a dry ice/ethanol bath. The capillaries were loaded into an EN 5107D2 resonator, and Q-band measurements were performed at 80 K on a Bruker Elexsys 580 spectrometer with a Super Q-FTu Bridge. For the four-pulse DEER experiment used here, a 32-ns π-pump pulse was applied to the low field peak of the nitroxide field-swept spectrum, and the observer π/2 (16 ns) and π (32 ns) pulses were positioned 50 MHz (17.8 G) upfield, which corresponds to the nitroxide centre line. Distance distributions were obtained from the raw dipolar evolution data using the LabVIEW (National Instruments) 'LongDistances' program, developed by C. Altenbach, which can be downloaded from http://www.biochemistry.ucla.edu/Faculty/Hubbell/.

Phage display selections.

Avi-tagged heterotrimeric G_i was used for biopanning during selection. The G_i construct has an Avitag on the N-terminal end of the gamma subunit ($G\gamma$). The Avitag was biotinylated in vivo in Sf9 cells by co-expression of the biotin ligase BirA in presence of supplemented D-biotin. Pull-down experiments on Streptavidin magnetic beads showed quantitative biotinylation of the trimeric complex used in selection. Phage display selection was performed according to published protocols[48]. In brief, in the first round, 200 nM of target was immobilized on 250 μl magnetic beads. Then, 100 μl of a phage library[49] containing 10^{12}–10^{13} virions were added to the Streptavidin beads and incubated for 30 min. The resuspended beads containing bound virions were washed extensively and then used to infect freshly grown log phase *Escherichia coli* XL1-Blue cells. Phages were amplified overnight in 2xYT media (Fisher Scientific) with 50 μg ml^{-1} ampicillin and 10^9 p.f.u. ml^{-1}

of M13-KO7 helper phage. To increase the stringency of selection, three additional rounds of sorting were performed with decreasing the target concentration in each round (second round: 50 nM, third round: 10 nM and fourth round: 10 and 5 nM) using the amplified pool of virions of the preceding round as the input. Sorting from the second to fourth rounds was done on a Kingfisher instrument. From the second to fourth rounds, the targets were premixed with the amplified phage pool and then Streptavidin beads were added to the mixture. From the second round onwards, the bound phages were eluted using 0.1 M glycine, pH 2.7. This technique often risks the elution of non-specific and Streptavidin binders, which tend to overpopulate the amplified phage pool thereby reducing the chance to obtain the desired specific clones. To eliminate them, the precipitated virions from the second round onwards were negatively selected against 100 μl of Streptavidin beads. The pre-cleared phage pool was then used as an input for the selection.

Single-point phage ELISA.

All ELISA experiments were performed in 96-well plates coated with 50 μl of 2 μg ml^{-1} neutravidin in Na_2CO_3 buffer, pH 9.6 and subsequently blocked by 0.5% BSA in PBS. A single-point phage ELISA was used to rapidly screen the binding of the obtained Fab fragments in phage format. Colonies of *E. coli* XL1-Blue harbouring phagemids were inoculated directly into 500 μl of 2xYT broth supplemented with 100 μg ml^{-1} ampicillin and M13-KO7 helper phage. The cultures were grown at 37 °C for 16–20 h at 280 r.p.m. in a 96-deep-well block plate. Culture supernatants containing Fab phage were diluted tenfold in PBST buffer. After 15 min of incubation, the mixtures were transferred to ELISA plates that were incubated with 50 nM biotinylated trimeric G_{i1} in experimental wells and with buffer in control wells for 15 min. The ELISA plates were incubated with the phage for another 15 min and then washed with PBST. The washed ELISA plates were incubated with horseradish perixoidase (HRP)-conjugated anti-M13 mouse monoclonal antibody (ab50370, Abcam,1:5,000 dilution in PBST) for 30 min. The plates were again washed, developed with TMB substrate and then quenched with 1.0 M HCl, and the absorbance at 450 nm was determined. The background binding of the phage was monitored by the absorbance from the control wells.

Sequencing, cloning, overexpression and purification of Fab fragments.

From phage ELISA, clones (selected based on a high ratio of ELISA signal of target binding to background) were sequenced at the DNA Sequencing Facility at the University of Chicago. Unique clones were sub-cloned in pRH2.2, an IPTG inducible vector for expression of Fabs in *E. coli*. *E. coli* BL21 (Gold) cells were transformed with sequence-verified clones of Fab fragments in pRH2.2. Fab fragments were grown in 2xYT media with 100 μg ml^{-1} ampicillin at 37 °C for 2–2.5 h, during which $A_{600\ nm}$ reached 0.6–0.8, induced with 1 mM IPTG and grown for a further 4.5 h at 37 °C. Harvested cells were kept frozen at −80 °C until use. Frozen pellets were re-suspended in PBS supplemented with 1 mM PMSF, and 1 μg ml^{-1} DNase I. The suspension was lysed by ultrasonication. The cell lysate was incubated at 65 °C for 30 min to eliminate of any undesired proteolysed fragments of the Fab produced during overexpression. Heat-treated lysate was then cleared by centrifugation, filtered through 0.22 μm filter and loaded onto a HiTrap MabSelect SuRe 5-mL column pre-equilibrated with lysis buffer (20 mM phosphate buffer, pH 7.5, 500 mM NaCl). The column

was washed with 10 column volumes of lysis buffer followed by elution of Fab fragments with elution buffer (0.1 M acetic acid). Fractions containing protein were directly loaded onto a Resource S 1-mL column pre-equilibrated with buffer A (50 mM sodium acetate, pH 5.0) followed by washing with 10 column volumes wash with buffer A. Fab fragments were eluted with a linear gradient 0–50% of buffer B (50 mM sodium acetate, pH 5.0, 2.0 M NaCl). Affinity and ion-exchange chromatography were performed using an automated program on ÄKTA explorer system. Purified Fab fragments were dialysed overnight against 20 mM HEPES, pH 7.4, 150 mM NaCl. The quality of purified Fab fragments was analysed by SDS–PAGE.

Rhodopsin–G_i–Fab complex formation and purification.

Sf9 cell pellets infected with virus containing rhodopsin were lysed in 20 mM HEPES, pH 7.2, 10 mM NaCl, and 10 mM $MgCl_2$. The supernatant was centrifuged at 160,000*g* for 30 min to collect the membranes. The membranes were washed by homogenization in 20 mM HEPES, pH 7.2, 1 M NaCl and 10 mM $MgCl_2$, and then was collected by centrifugation at 160,000*g* for 30 min.

The rhodopsin–G_i complex was formed in membranes as described previously[15]. The washed membranes were re-suspended in 20 mM HEPES, pH 7.2, 100 mM NaCl, 10% glycerol, and 5 μM ATR. For 1 l of rhodopsin cell pellets, 6 mg of G_i 10 mg Fab_G50 and 1 U of apyrase were added. The sample was incubated overnight at 4 °C. The membranes were then solubilized in 20 mM HEPES, pH 7.2, 100 mM NaCl, 10% glycerol, 0.5% DDM (Anatrace), 0.1% cholesteryl hemisuccinate (CHS), and 5 μM ATR for 2 h at 4 °C. The supernatant was isolated by centrifugation at 160,000*g* for 1 h, and then was incubated with TALON IMAC resin (Clontech) for 3 h at 4 °C. After binding, the resin was washed with 10 column volumes of 20 mM HEPES, pH 7.2, 100 mM NaCl, 0.02% DDM, 0.004 CHS, 50 mM imidazole and 5 μM ATR. The buffer was exchanged to 20 mM HEPES, pH 7.2, 100 mM NaCl, 0.1% digitonin and 5 μM ATR. The protein was then treated overnight with His-tagged TEV protease (made in-house) on column. The complex sample was eluted with 20 mM HEPES, pH 7.2, 100 mM NaCl, 0.1% digitonin, 50 mM imidazole and 5 μM ATR. The rhodopsin–G_i–Fab complex sample was concentrated and loaded onto Superdex S200 10/300 GL column with running buffer 20 mM HEPES, pH 7.2, 100 mM NaCl, 0.1% digitonin and 5 μM ATR; the fractions for the monomeric complex were collected and concentrated individually for electron microscopy experiments.

Negative-stain analysis of rhodopsin–G_i–Fab complex.

Protein samples were applied to a freshly glow-discharged carbon coated copper grid and allowed to adhere for 10 s before being reduced to a thin film by blotting. Immediately after blotting, 3 μl of a 1% solution of uranyl formate was applied to the grid and blotted off directly. This was repeated three times. Data were acquired using a Tecnai Spirit transmission electron microscope operating at 120 kV. Images were processed using Relion 2.1[50].

Cryo-EM data acquisition.

A droplet (2.75 μl) of purified rhodopsin–G_i–Fab complex at a concentration of about 9 mg ml^{-1} was applied to a glow-discharged holey carbon grid (Quantifoil R1.2/1.3, Au 300 mesh), and subsequently vitrified using a Vitrobot Mark IV (FEI Company). Cryo-EM data were collected on a Titan Krios microscope using a K2 camera positioned post a GIF quantum energy filter, with a slit width of 20 eV. Micrographs were recorded in super-resolution mode at a magnified physical pixel size of 1.074 Å, with defocus values ranging from −1.3 to −3.0 μm. The total exposure time was set to 6 s with intermediate frames recorded every 0.2 s, resulting in an accumulated dose of about 60 electrons per $Å^2$ and a total of 30 frames per movie stack.

Image processing and structural refinement.

In the initial phase of processing, unbinned image stacks from 19,368 K2 movies were corrected for drift and for beam-induced motion by alignment using cross-correlation as implemented in Unblur[51]. Dose-corrected integrated frames were used for subsequent image processing. Particles were automatically picked using RELION 2.1[50] using 6 projection image references, generated by applying 2D classification on 1,000 manually picked particles. CTFFIND4 was used for CTF estimation[52]. Next, a set of 1.65 million particles were extracted from the 14,464 integrated frames displaying Thon rings extending beyond 4.5 Å. The extracted particle images were normalized, and subjected to 50 rounds of both iterative 2D classification (regularization parameter $T = 2$) and 3D classification ($T = 4$). Uninterpretable, sparsely populated, or poorly defined classes were discarded at both stages leaving behind approximately 227 k particles for further 3D processing (Extended Data Fig. 3). A coarse initial model was generated using the 3D initial model generation module in RELION and the model was refined until convergence was achieved. Density maps were corrected with a *B*-factor of −217 and ‘gold-standard’ Fourier shell correlation (FSC) resolution plots were calculated with a soft shape mask applied to independent, unfiltered half-maps resulting from the processing.

The crystal structure of human rhodopsin (PDB code 4ZWJ) and G protein complex (PDB code 1GG2) were used as initial models for model rebuilding and refinement against the electron microscopy map. All models were docked into the electron microscopy density map using Chimera[53], followed by iterative manual adjustment in COOT[54], fragment-based refinement with Rosetta[55], and real space refinement using Phenix programs[56]. The model statistics was validated using MolProbity[57]. Structural figures were prepared in Chimera and PyMOL (https://pymol.org/2/). The final refinement statistics are provided in Supplementary Table 3. The extent of any model overfitting during refinement was measured by refining the final model against one of the half-maps and by comparing the resulting map versus model FSC curves with the two half-maps and the full model.

In-cell disulfide bond cross-linking.

The open-reading frames of mini-Gi with an N-terminal Flag tag and full-length rhodopsin with a C-terminal haemagglutinin (HA) tag were cloned into pcDNA6. Cysteine mutations (E28C for miniG_i and N145C or F146C for rhodopsin) were systematically introduced in these two DNA vectors. AD293 cells were split 1 day before transfection at 50,000 cells per

well in a 24-well plate. Cells were grown for 1 day, then transfected with 100 ng rhodopsin constructs (pcDNA6-rho-3HA) plus 100 ng G_i plasmid (pcDNA6–3xFlag-miniGi), 100 ng pcDNA6-Gβ, and 100 ng pcDNA6-Gγ by Lipofectamine 2000 (DNA:Lipofectamine 2000 ratio of 1:2) in each well. Cells were grown for 2 days after transfection, and were then treated at room temperature with H_2O_2, which was freshly diluted in the cell culture medium to a final concentration of 1 mM. After 5 min of treatment with H_2O_2, the medium was aspirated and 100 μl of CelLytic M (Sigma C2978) were added to each well and the plate was shaken for 10 min at room temperature. Cell lysates were transferred to a 1.5 ml tubes, spun at 18,000*g* at 4 °C for 5 min. The supernatants (10 μl) were mixed with an equal volume of 2× SDS loading buffer (without reducing agents) for 5 min at room temperature, and loaded onto a protein gel for western blot analysis. HRP-conjugated anti-Flag (A8592, Sigma) and anti-HA (H3663, Sigma) antibodies were used to probe for free and cross-linked miniGi and rhodopsin proteins.

$G\alpha_i$-mediated ERK activation assay and cAMP accumulation assay.

AD293 cells were plated at a density of 5×10^4 per well in 24-well plates 1 day before transfection. Cells were then transiently transfected using Lipofectamine 2000 reagent (Life Technologies) with 50 ng cDNA encoding GPCR, 200 ng luciferase reporter construct containing an ERK response element (SRE) or cAMP response element (CRE), and 10 ng TK-*Renilla* at a Lipofectamine 2000 reagent:DNA ratio of 2:1. ERK activation or cAMP accumulation was detected using the Dual-luciferase reporter assay system from Promega according to the manufacturer's instructions using an EnVision plate reader (Perkin Elmer). *Renilla* luciferase was used for normalization. All experiments were performed in triplicate, with each well transfected independently.

Molecular dynamics simulation setup and equilibration.

Molecular dynamics simulations of two G_i couplers, rhodopsin (PDB code 3PQR) and mOR1 (PDB code 5C1M), and two G_s couplers, β_2AR (PDB code 4LDE) and A_{2A}R (PDB code 5G53), were initiated from structures in the active (S4) conformation as described previously[58]. All receptors selected met the following inclusion criteria: a fully active, agonist-bound receptor in complex with a peptide, nanobody, or engineered G protein, and free of any ICL3 fusion that may influence the conformational state of the receptor.

Each receptor was prepared for simulations as follows. Crystallization partners and heteroatoms, with exception of agonists bound within the orthosteric binding site and palmitoylated cysteine residues on helix 8, were removed. Thermostabilizing and non-native mutations were reverted back to their wild-type residue and missing residues not within ICL3 were modelled and subjected to 5,000 rounds of 'very_slow' loop refinement assed by DOPE scoring using Modeller 9.17[59]. Palmitoyl groups on helix 8 were then added and protonation states for active receptors were assigned based on previous publications[45,60,61]. The resulting complexes were capped with neutral acetyl and methylamine groups and embedded into a pre-equilbirated palmitoyl-oleoyl-phosphatidylcholine (POPC) lipid bilayer, solvated in a box of TIP3P waters allowing for 14 Å of padding on all sides with 150 mM NaCl, and neutrailized by removing appropriate ions or counter ions using the Desmond system builder within Maestro (Schrödinger Release 2018–1: Maestro,

Schrödinger, LLC, New York, 2018). Full details for each system can be found in Supplementary Table 1.

All-atom atmospheric simulations were performed using GROMACS5.0.6 with the CHARMM36m force field and periodic boundary conditions[62]. Ligand parameters were generated by SwissParam[63]. Before production simulations, 50,000 steps of energy minimization were performed, followed by equilibration in the canonical (NVT) and isothermal–isobaric (NPT) ensembles for 10 and 50 ns, respectively, with positional restraints (1,000 kJ mol^{-1} nm^{-2}) placed on backbone atoms. Temperature was maintained at 310 K using the v-rescale method with a coupling time of 0.1 ps and pressure was maintained at 1 bar using the Berendsen barostat with a coupling time (t_p) of 1.0 ps and compressibility of 4.5×10^{-5} bar^{-1} with a 2 fs timestep[64].

Mollified adaptive biasing potential simulations.

To calculate the free energy landscape of TM6 movement relative to the transmembrane bundle of the receptor, we used mABP with overfill protection using fABMACS[65,66]. A centre-of-geometry (COG) distance collective variable was introduced into fABMACS and two collective variables were defined: COG distance between select TM6 (6.27–6.42) and TM1/2 (1.50–1.59 and 2.39–2.48) C_α atoms, and COG distance between select TM6 and TM3/4 (3.45–3.55 and 4.39–4.47) C_α atoms (Extended Data Fig. 7). The collective variable space was discretized into a 480 × 480 grid with ranges of 0 to 50 Å for a bin width of 0.10 Å. Biasing parameters were $b = 0.8$, $c = 0.01/\delta t$, $a = 10$, and a maximum fill level of 30 kJ mol^{-1}. Simulation parameters for mABP simulations were the same as those used during NPT equilibration except the Parrinello–Rahman barostat with a 5.0 ps coupling time was used. To prevent unwanted transitions away from the active conformation of the receptors, the NPXXY tyrosine was held in an active conformation and TM7 was restrained using Urey–Bradley harmonic potentials between residues 7.42–7.53, in which angles and distances were derived from the equilibrated structure and residues i, j, k of the potential were i, $i + 2$, $i + 4$. Simulations without TM7 restraints saw quick transitions towards receptor inactivation, consistent with prior long time scale simulations[67] (data not shown). For simulations in which ICL3 was truncated or not resolved, backbone distance restraints were placed on the last four residues to prevent helical unwinding. Independent mABP production simulations for each receptor were run in duplicate for approximately 12 μs in total. Throughout the simulations, the instantaneous boost was recorded for each recorded frame allowing for the generation of weighted histograms. Simulation analysis was performed using MDTraj 1.7.2 and VMD 1.9.2[1,7]. Plots were generated using the R statistical package.

Reporting summary.

Further information on experimental design is available in the Nature Research Reporting Summary linked to this paper.

Data availability.

All data and source code are available upon request.

Extended Data

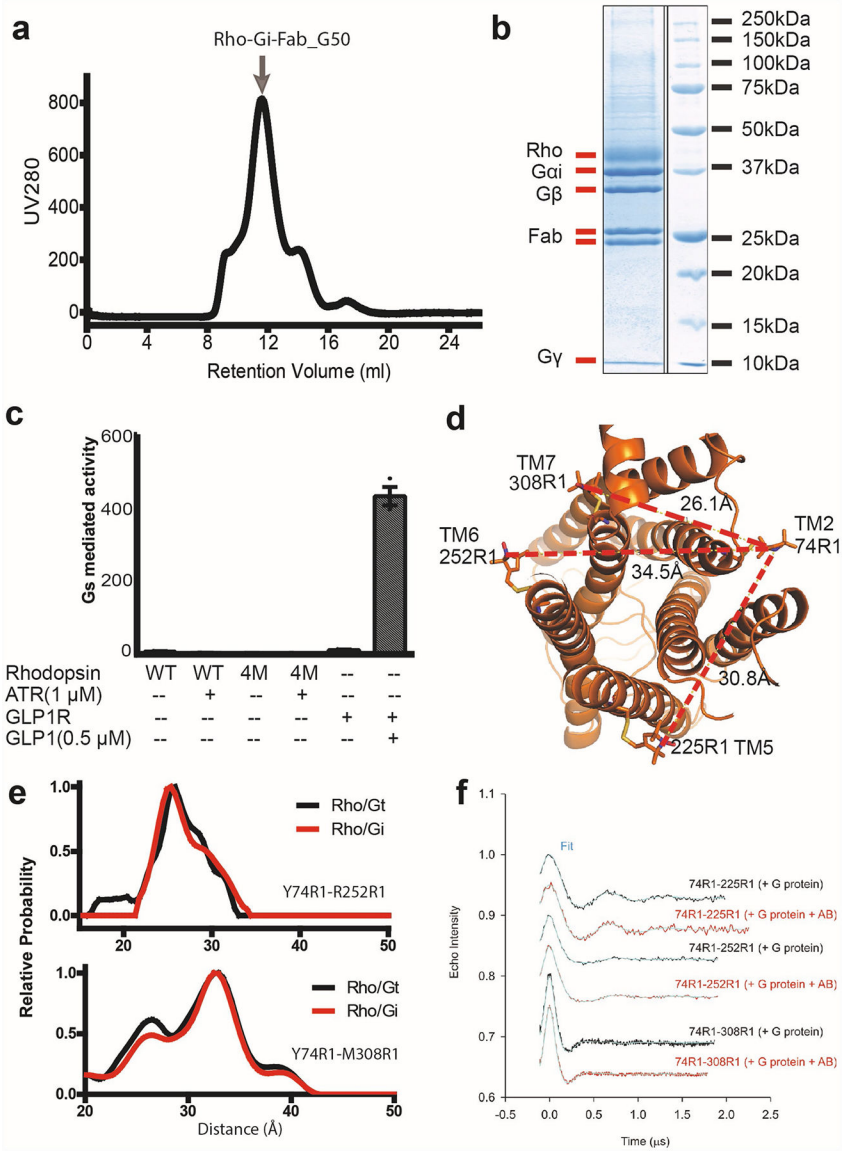

Extended Data Fig. 1 |. Purification, characterization and cryo-EM images of the Rho–G_i–Fab complex.

a, Representative elution profile of the purified Rho–G_i–Fab_G50 complex on Superdex 200 10/300 gel filtration. **b**, SDS–PAGE analysis of the complex after gel filtration. **c**, The inability of rhodopsin to stimulate the G_s-mediated signalling as assayed by the cAMP-driven luciferase reporter assays. The glucagon-like peptide 1 receptor (GLP-1R) shows stronger G_s-meditated signalling with the agonist GLP-1 (n = 3 independent experiments). Data are mean ± s.d. **d**, An overall view of rhodopsin showing the three intramolecular distances between two nitroxide N–O bonds based on the models of the R1 nitroxide pairs Y74R1-Q225R1, Y74R1-R252R1 and Y74R1-M308R1, respectively ($Y74^{2.41}$, $Q225^{5.60}$, $R252^{6.35}$, $M308^{7.55}$; superscripts denote Ballesteros–Weinstein numbering). R1 side-chain modelling details have been described previously[27]. **e**, Similar DEER distance distributions

of TM6 and TM7 to TM2 of rhodopsin bound to G_i and G_t. **f**, Time domain data of DEER measurements.

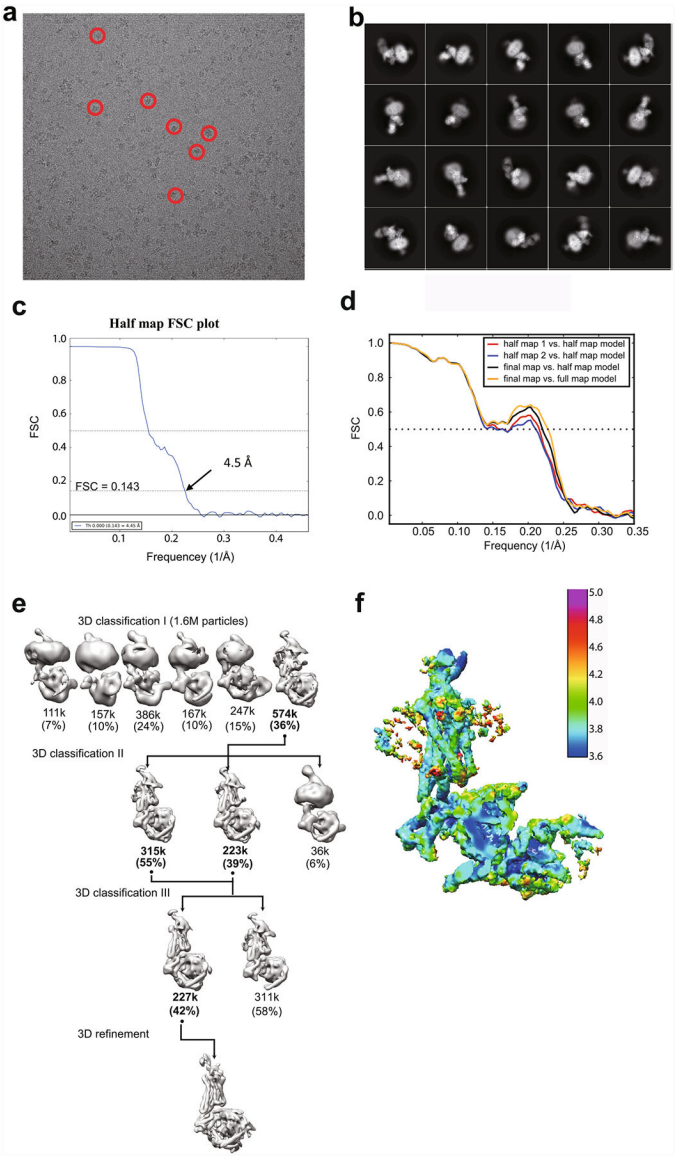

Extended Data Fig. 2 |. Cryo-EM images and single-particle analysis of the Rho–G_i–Fab complex.

a, Representative cryo-EM micrograph of Rho–G_i–Fab complex. Examples of particle projections are circled. **b**, Reference-free two-dimensional class averages of the complex in digitonin micelles. **c**, Half-map Fourier shell correlation (FSC) plots as produced by RELION with the mask used shown as an inset. **d**, FSC curve of model versus the full map, as well as FSC curves obtained for a model refined against a half-map and compared to the two half-maps as well as the full model. The r.m.s.d. between the model refined against half-map and compared to the full map, and the one refined against the full map is 0.984 Å, and their corresponding FSCs against the final map show a resolution difference at the 0.5-cutoff

of approximately 0.1 Å. **e**, Particle classification and refinement. **f**, Local resolution map of the rhodopsin–G_i complex.

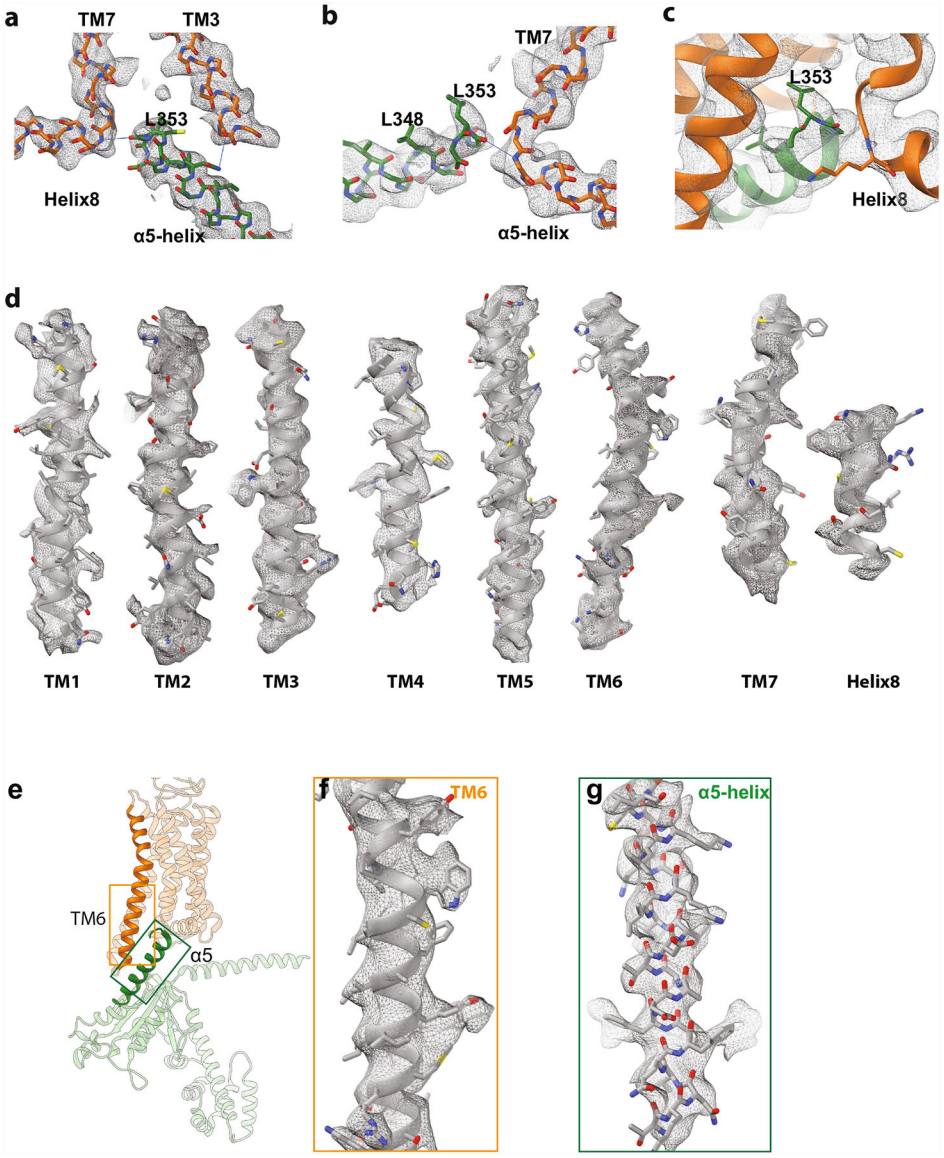

Extended Data Fig. 3 |. Electron microscopy density map of rhodopsin–G_i complex.
a–**c**, Three views of the electron microscopy density map of the rhodopsin–$G\alpha_i$ interface. **d**, Electron microscopy density map of all rhodopsin transmembrane helices and helix 8. **e**–**g**, An overall view of the rhodoposin–$G\alpha_i$ interface (**e**), and electron microscopy density map for the TM6 of rhodopsin (**f**) and the α5-helix of $G\alpha_i$ (**g**).

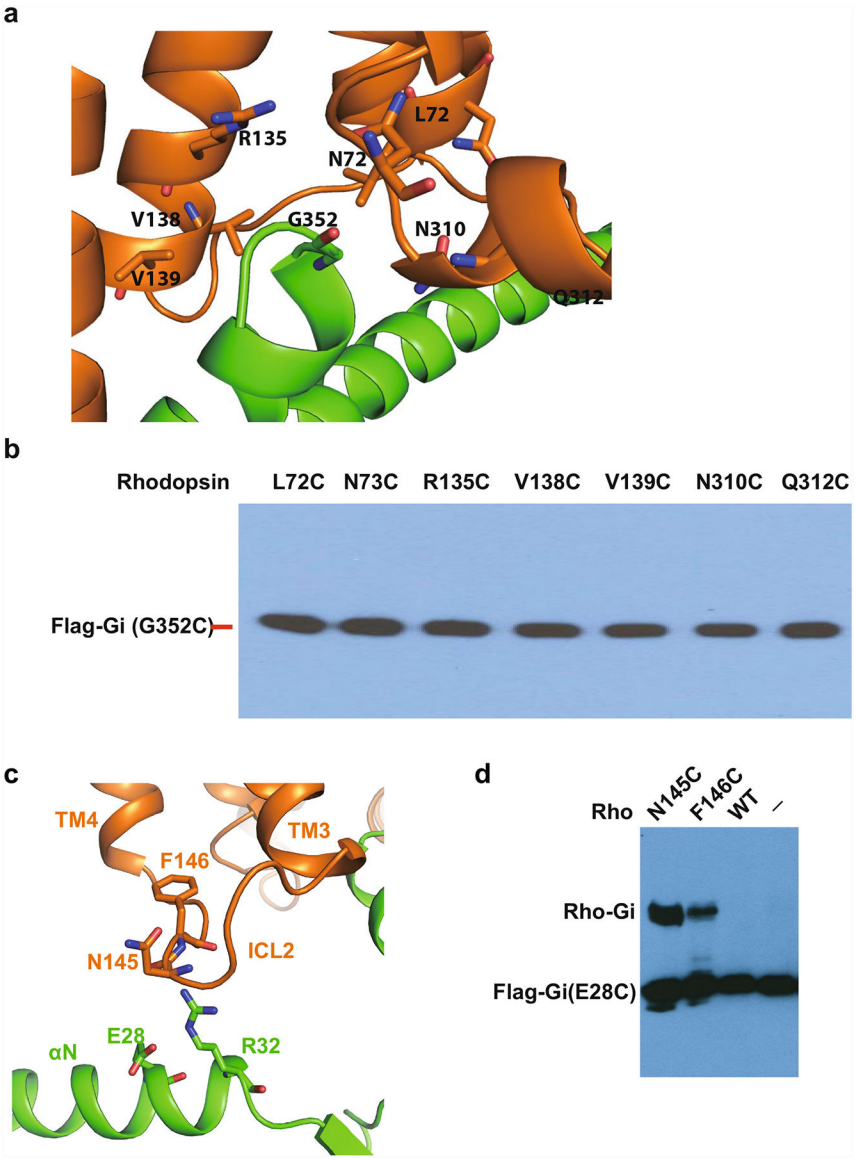

Extended Data Fig. 4 |. The rhodopsin–G_i interface and disulfide crosslinking of rhodopsin with $G\alpha_i$.

a, The rhodopsin–G_i interface surrounding the G352 residue of $G\alpha_i$ α5-helix. Not all side chains shown are visible in the map but shown here for illustrating their C_α positions to facilitate understanding of data in panel **b**. **b**, Lack of disulfide crosslinking of G352C of G_i with surrounding residues from rhodopsin (compare with **d**; $n = 3$ independent experiments). **c**, Interactions at the interface between ICL2 of rhodopsin and αN helix of $G\alpha_i$. The side chains are not visible in the map but shown here for illustrating their C_α positions. **d**, Demonstration that E28C of $G\alpha_i$ can be disulfide cross-linked to rhodopsin residues $N145C^{ICL2}$ and $F146C^{ICL2}$ ($n = 3$ independent experiments).

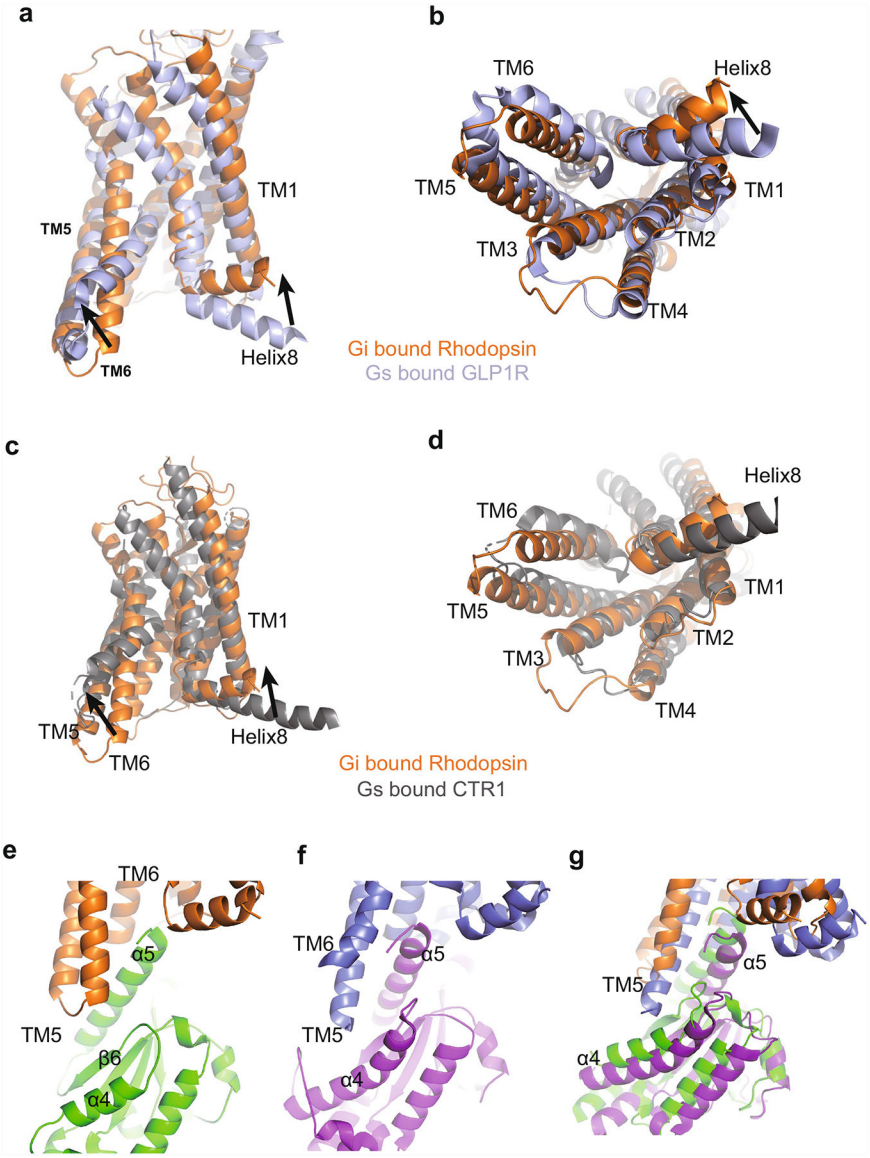

Extended Data Fig. 5 |. Structural comparison of G_i-bound rhodopsin, G_s-bound GLP-1R, and G_s-bound CTR, and the role of α4-helix of Gα in receptor selectivity.

a, **b**, Side and cytoplasmic views of G_i-bound rhodopsin (orange) overlaid with G_s-bound GLP-1R (PDB code 5VAI, light blue, black arrows indicate differences in helix positions). **c**, **d**, Side and cytoplasmic views of G_i-bound rhodopsin (orange) overlaid with G_s-bound CTR (PDB code 5UZ7, grey). **e**, **f**, Side-by-side comparison of the rhodopsin–G_i complex (**e**) with the β_2AR–G_s complex (**f**). **g**. An overlay of the rhodopsin–G_i complex with the β_2AR–G_s complex reveals possible collision of TM5 of β_2AR with α4-helix of $G\alpha_i$.

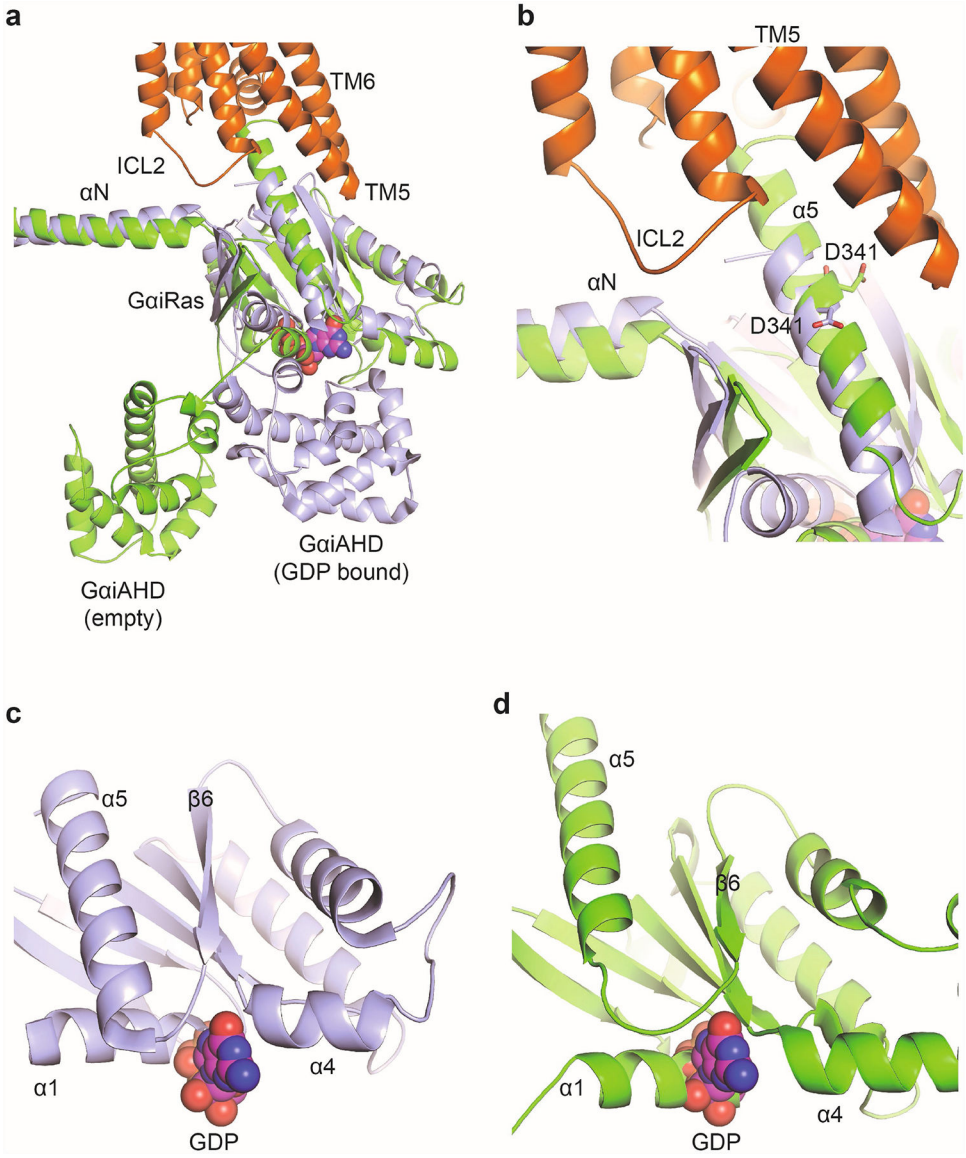

Extended Data Fig. 6 |. The mechanism of rhodopsin-mediated G_i activation.

a, **b**, Superposition of the rhodopsin–G_i complex with the inactive GDP-bound G_i (PDB code 1GG2) reveals separation of the AHD from the Ras domain of $G\alpha_i$ (**a**) and conformational changes in the α5-helix (**b**). **c**, **d**, Side-by-side comparison of the GDP-binding site of the $G\alpha_i$ Ras domain in the inactive GDP-bound $G\alpha_i$ (**c**) and nucleotide-free state $G\alpha_i$ with GDP added for comparison (**d**).

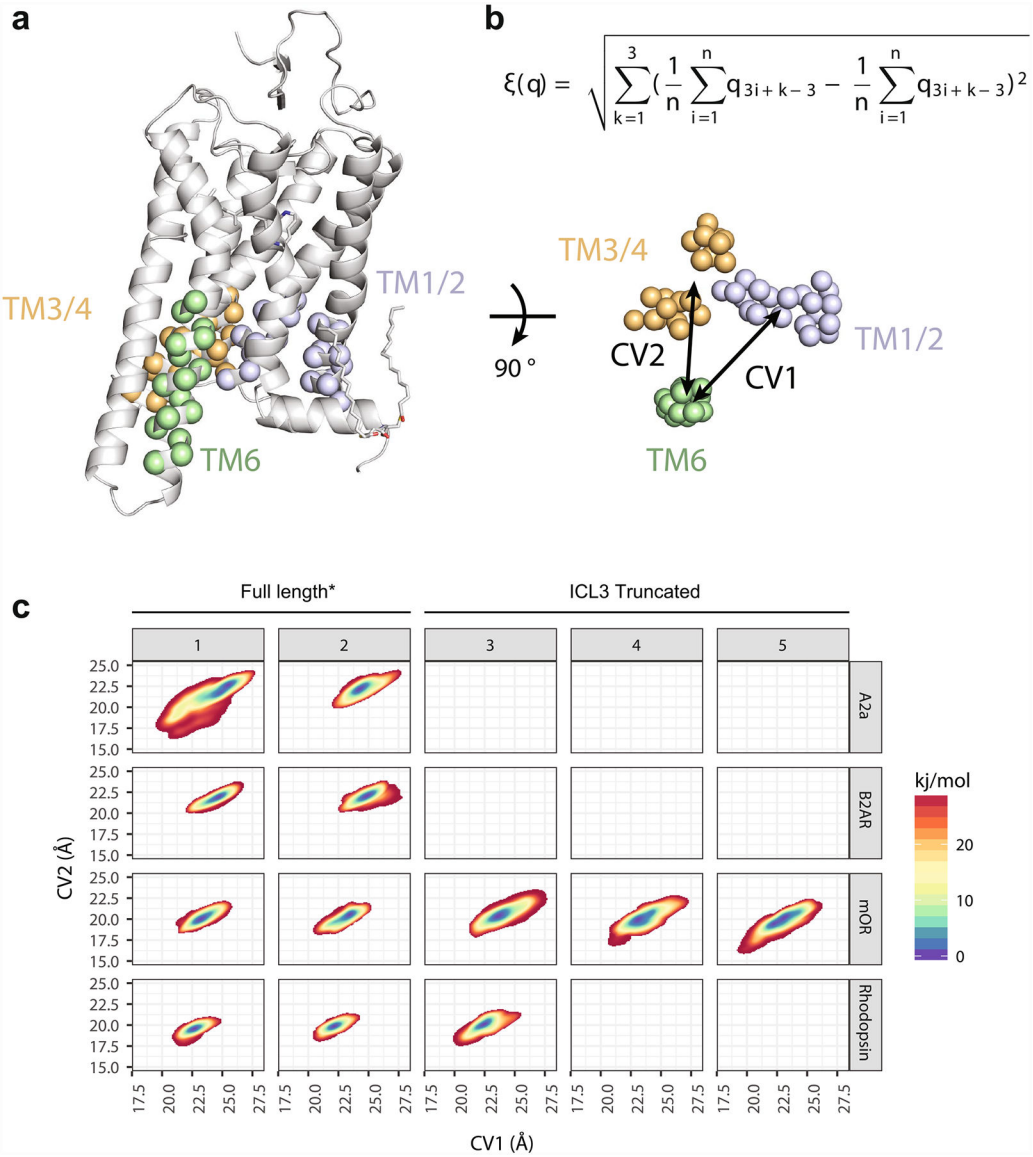

Extended Data Fig. 7 |. Collective variables for mABP simulations and free-energy landscapes of mABP simulations.

a, To bias movement between TM6 relative to that of the receptor bundle, two centre-of-geometry (COG) distance collective variables (CVs) were implemented into fABMACS[66]. CV1 and CV2 are COG distances between selected atoms of TM6 to TM1/2 and TM6 to TM3/4 respectively. Collective variable atoms for the rhodopsin simulation are highlighted. **b**, COG collective variable formula and the CV1 and CV2 distances. **c**, Potential energy surface reveals that CV1 and CV2 distances are larger in the G_s-coupled receptors ($A_{2A}R$ and β_2AR) than those in the G_i-coupled receptors (mOR1 and rhodopsin).

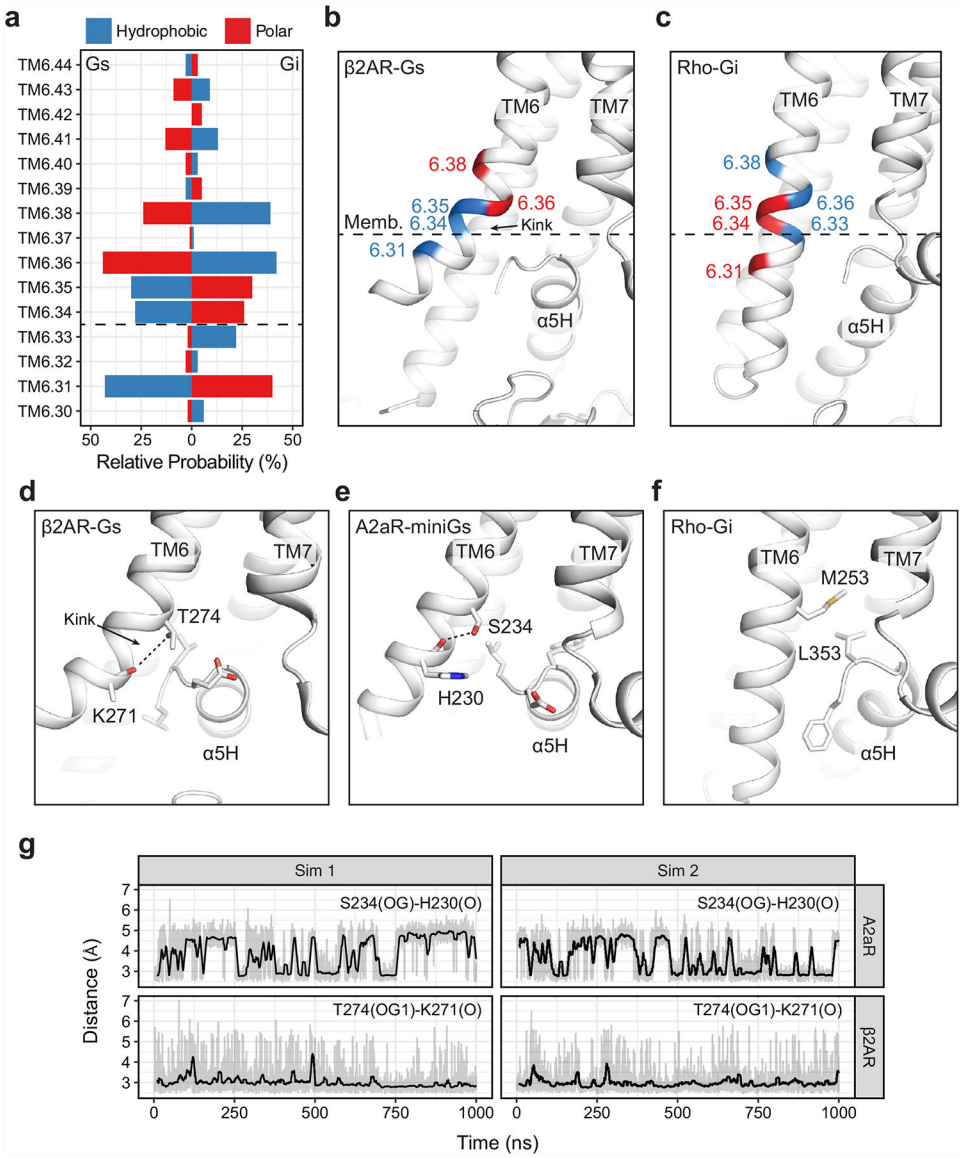

Extended Data Fig. 8 |. Enrichment profiles for G_i and G_s coupling receptors.

a–**c**, Relative probability of hydrophobic and polar residues for G_i ($n = 76$) and G_s ($n = 25$) coupling receptors. Residues with relative enrichments over 20% were mapped onto the structures of G_s-bound β_2AR (**b**) and G_i-bound rhodopsin (**c**). GPCR principal coupling was previously defined[68]. **d**–**f**, Interaction network of TM6.36 of β_2AR, A_{2A}R and rhodopsin with the G protein α5-helix. **g**, Hydrogen bonding between TM3.36 and the backbone of TM6.

Extended Data Table 1 |

Cryo-EM data collection, refinement and validation statistics

	#1 Rho-Gi (EMDB-7517) (PDB 6CMO)
Data collection and processing	
Magnification	45956
Voltage (kV)	300
Electron exposure (e–/Å^2)	60
Defocus range (μm)	−1.5 to −2.5
Pixel size (Å)	1.074
Symmetry imposed	C1
Initial particle images (no.)	1656874
Final particle images (no.)	227386
Map resolution (Å)	4.5
FSC threshold	0.5
Map resolution range (Å)	3.6–5
Refinement	
Initial model used (PDB code)	
Model resolution (Å)	4.5
FSC threshold	0.143
Model resolution range (Å)	80–4.5
Map sharpening *B* factor (Å^2)	−217
Model composition	
Non-hydrogen atoms	11835
Protein residues	1518
Ligands	2
B factors (Å^2)	
Protein	129.9
Ligand	297.5
R.m.s. deviations	
Bond lengths (Å)	0.004
Bond angles (°)	1.001
Validation	
MolProbity score	1.23
Clashscore	4.5
Poor rotamers (%)	0.2
Ramachandran plot	
Favored (%)	98.67
Allowed (%)	1.33
Disallowed (%)	0

Extended Data Table 2 |

GPCR simulation systems used in the current study

Receptor (Coupling)	rhodopsin (Gi/t)	μ-opioid receptor 1 (Gi)	β2 adrenergic receptor (Gs)	adenosine A2A receptor (Gs)
PDB (resolution)	3PQR (2.85 Å)	5C1M (2.10 Å)	4LDE (2.79 Å)	5G53 (3.40 Å)
Crystallization Partner	Gt peptide	nanobody	nanobody	mini Gs
Ligand	ATR (agonist)	BU72 (agonist)	BI167107 (Agonist)	NEC (agonist)
System Size	77.2 Å × 77.2 Å × 97.0 Å; 10,610 waters; 128 POPC; 54,353 atoms total	79.1 Å × 79.1 Å × 93.3 Å; 10,347 waters; 135 POPC; 54,171 atoms total	81.1 Å × 81.1 Å × 89.2 Å; 10,198 waters; 143 POPC; 54,557 atoms total	90.2 Å × 90.2 Å × 89.7 Å; 12,720 waters; 191 POPC; 68,568 atoms total
Protonated Residues	D83$^{2.50}$, E113$^{3.28}$, E122$^{3.37}$, E134$^{3.49}$	D116$^{2.50}$	D79$^{2.50}$, E122$^{3.41}$, D130$^{3.49}$	D52$^{2.50}$,D101$^{3.49}$
Palmitoylation	C322, C323		C341	
Simulations	Sim 1: 0.89 μs Sim 2: 0.90 μs Sim 3^{t}: 1.00 μs	Sim 1: 0.98 μs Sim 2: 0.98 μs Sim 3^{t}: 1.00 μs Sim 4^{t}: 1.00 μs Sim 5^{t}: 1.00 μs	Sim 1: 1.00 μs Sim 2: 1.00 μs	Sim 1: 1.00 μs Sim 2: 1.00 μs

Simulations marked with a superscript ‘t’ indicate truncation of a crystallographically resolved ICL3.

Supplementary Material

Refer to Web version on PubMed Central for supplementary material.

Acknowledgements

Cryo-EM data were collected at the David Van Andel Advanced Cryo-Electron Microscopy Suite in the Van Andel Research Institute. This work was supported in part by the National Institutes of Health grant, DK071662, American Asthma Foundation, Jay and Betty Van Andel Foundation, Ministry of Science and Technology (China) grants 2012ZX09301001 and 2012CB910403, 2013CB910600, XDB08020303, 2013ZX09507001 (to H.E.X.), GM117372 (to A.K.), GM0875119 (to A.A.K.), grant from Pfizer (to A.A.K.), the National Natural Science Foundation 31770796 (to Y.J.), the Canada Excellence Research Chairs program (to O.P.E.), the Canadian Institute for Advanced Research (to O.P.E.), the Anne and Max Tanenbaum Chair in Neuroscience (to O.P.E.), by funds from the Center for Cancer Research, National Cancer Institute, NIH, Bethesda, MD (to S.S.), and by federal funds from the Frederick National Laboratory for Cancer Research, National Institutes of Health, under contract HHSN261200800001E. We thank H. Li and W. Lü for help with analysing the cryo-EM data and for advice on refinement, L. Bai and Z. Yuan for advice on 3D reconstruction, V. Falconieri for assistance with figure preparation, the HPC team at VARI for computational support, D. Nadziejka for manuscript editing, and B. Dickson for consultation on molecular dynamics simulation.

References

1. Fredriksson R, Lagerström MC, Lundin LG & Schiöth HB The G-protein-coupled receptors in the human genome form five main families. Phylogenetic analysis, paralogon groups, and fingerprints. Mol. Pharmacol 63, 1256–1272 (2003). [PubMed: 12761335]
2. Neves SR, Ram PT & Iyengar R G protein pathways. Science 296, 1636–1639 (2002). [PubMed: 12040175]
3. Gurevich EV & Gurevich VV Arrestins: ubiquitous regulators of cellular signaling pathways. Genome Biol. 7, 236 (2006). [PubMed: 17020596]
4. Zhou XE, Melcher K & Xu HE Understanding the GPCR biased signaling through G protein and arrestin complex structures. Curr. Opin. Struct. Biol 45, 150–159 (2017). [PubMed: 28558341]

5. Palczewski K et al. Crystal structure of rhodopsin: a G protein-coupled receptor. Science 289, 739–745 (2000). [PubMed: 10926528]
6. Cherezov V et al. High-resolution crystal structure of an engineered human β_2-adrenergic G protein-coupled receptor. Science 318, 1258–1265 (2007). [PubMed: 17962520]
7. Rosenbaum DM et al. GPCR engineering yields high-resolution structural insights into beta2-adrenergic receptor function. Science 318, 1266–1273 (2007). [PubMed: 17962519]
8. Xu F et al. Structure of an agonist-bound human A_{2A} adenosine receptor. Science 332, 322–327 (2011). [PubMed: 21393508]
9. Lebon G et al. Agonist-bound adenosine A_{2A} receptor structures reveal common features of GPCR activation. Nature 474, 521–525 (2011). [PubMed: 21593763]
10. Choe HW et al. Crystal structure of metarhodopsin II. Nature 471, 651–655 (2011). [PubMed: 21389988]
11. Wang C et al. Structural basis for molecular recognition at serotonin receptors. Science 340, 610–614 (2013). [PubMed: 23519210]
12. Standfuss J et al. The structural basis of agonist-induced activation in constitutively active rhodopsin. Nature 471, 656–660 (2011). [PubMed: 21389983]
13. Rosenbaum DM et al. Structure and function of an irreversible agonist–β_2 adrenoceptor complex. Nature 469, 236–240 (2011). [PubMed: 21228876]
14. Rasmussen SG et al. Crystal structure of the β_2 adrenergic receptor–G_s protein complex. Nature 477, 549–555 (2011). [PubMed: 21772288]
15. Zhang Y et al. Cryo-EM structure of the activated GLP-1 receptor in complex with a G protein. Nature 546, 248–253 (2017). [PubMed: 28538729]
16. Liang YL et al. Phase-plate cryo-EM structure of a class B GPCR-G-protein complex. Nature 546, 118–123 (2017). [PubMed: 28437792]
17. Flock T et al. Selectivity determinants of GPCR–G-protein binding. Nature 545, 317–322 (2017). [PubMed: 28489817]
18. Palczewski K G protein-coupled receptor rhodopsin. Annu. Rev. Biochem 75, 743–767 (2006). [PubMed: 16756510]
19. Zhou XE, Melcher K & Xu HE Structure and activation of rhodopsin. Acta Pharmacol. Sin 33, 291–299 (2012). [PubMed: 22266727]
20. Hamm HE How activated receptors couple to G proteins. Proc. Natl Acad. Sci. USA 98, 4819–4821 (2001). [PubMed: 11320227]
21. Van Meurs KP et al. Deduced amino acid sequence of bovine retinal $G_{o\alpha}$: similarities to other guanine nucleotide-binding proteins. Proc. Natl Acad. Sci. USA 84, 3107–3111 (1987). [PubMed: 3106961]
22. Lerea CL, Somers DE, Hurley JB, Klock IB & Bunt-Milam AH Identification of specific transducin α subunits in retinal rod and cone photoreceptors. Science 234, 77–80 (1986). [PubMed: 3529395]
23. Kang Y et al. Crystal structure of rhodopsin bound to arrestin by femtosecond X-ray laser. Nature 523,561–567 (2015). [PubMed: 26200343]
24. Zhou XE et al. Identification of phosphorylation codes for arrestin recruitment by G protein-coupled receptors. Cell 170, 457–469 (2017). [PubMed: 28753425]
25. Maeda S et al. Crystallization scale preparation of a stable GPCR signaling complex between constitutively active rhodopsin and G-protein. PLoS One 9, e98714 (2014). [PubMed: 24979345]
26. Liu P et al. The structural basis of the dominant negative phenotype of the $G\alpha_{i1}\beta_1\gamma_2$ G203A/A326S heterotrimer. Acta Pharmacol. Sin 37, 1259–1272 (2016). [PubMed: 27498775]
27. Van Eps N et al. Conformational equilibria of light-activated rhodopsin in nanodiscs. Proc. Natl Acad. Sci. USA 114, E3268–E3275 (2017). [PubMed: 28373559]
28. Van Eps N et al. G_i- and G_s-coupled GPCRs show different modes of G-protein binding. Proc. Natl Acad. Sci. USA 10.1073/pnas.1721896115 (2018).
29. Oldham WM, Van Eps N, Preininger AM, Hubbell WL & Hamm HE Mechanism of the receptor-catalyzed activation of heterotrimeric G proteins. Nat. Struct. Mol. Biol 13, 772–777 (2006). [PubMed: 16892066]

30. Oldham WM & Hamm HE Heterotrimeric G protein activation by G-protein-coupled receptors. Nat. Rev. Mol. Cell Biol 9, 60–71 (2008). [PubMed: 18043707]
31. Marin EP, Krishna AG & Sakmar TP Rapid activation of transducin by mutations distant from the nucleotide-binding site: evidence for a mechanistic model of receptor-catalyzed nucleotide exchange by G proteins. J. Biol. Chem 276, 27400–27405 (2001). [PubMed: 11356823]
32. Marin EP, Krishna AG & Sakmar TP Disruption of the α5 helix of transducin impairs rhodopsin-catalyzed nucleotide exchange. Biochemistry 41, 6988–6994 (2002). [PubMed: 12033931]
33. Garcia PD, Onrust R, Bell SM, Sakmar TP & Bourne HR Transducin-α C-terminal mutations prevent activation by rhodopsin: a new assay using recombinant proteins expressed in cultured cells. EMBO J. 14, 4460–4469 (1995). [PubMed: 7556089]
34. Onrust R et al. Receptor and βγ binding sites in the alpha subunit of the retinal G protein transducin. Science 275, 381–384 (1997). [PubMed: 8994033]
35. Skiba NP, Bae H & Hamm HE Mapping of effector binding sites of transducin alpha-subunit using $G\alpha_t/G\alpha_{i1}$ chimeras. J. Biol. Chem 271, 413–424 (1996). [PubMed: 8550597]
36. Sun D et al. Probing $G\alpha_{i1}$ protein activation at single-amino acid resolution. Nat. Struct. Mol. Biol 22, 686–694 (2015). [PubMed: 26258638]
37. Itoh Y, Cai K & Khorana HG Mapping of contact sites in complex formation between light-activated rhodopsin and transducin by covalent crosslinking: use of a chemically preactivated reagent. Proc. Natl Acad. Sci. USA 98, 4883–4887 (2001). [PubMed: 11320238]
38. Subramaniam S, Gerstein M, Oesterhelt D & Henderson R Electron diffraction analysis of structural changes in the photocycle of bacteriorhodopsin. EMBO J. 12, 1–8 (1993). [PubMed: 8428572]
39. Subramaniam S & Henderson R Molecular mechanism of vectorial proton translocation by bacteriorhodopsin. Nature 406, 653–657 (2000). [PubMed: 10949309]
40. Slessareva JE et al. Closely related G-protein-coupled receptors use multiple and distinct domains on G-protein α-subunits for selective coupling. J. Biol. Chem 278, 50530–50536 (2003). [PubMed: 14525988]
41. Kling RC, Lanig H, Clark T & Gmeiner P Active-state models of ternary GPCR complexes: determinants of selective receptor–G-protein coupling. PloS One 8, (2013).
42. DeVree BT et al. Allosteric coupling from G protein to the agonist-binding pocket in GPCRs. Nature 535, 182–186 (2016). [PubMed: 27362234]
43. Dror RO et al. Signal transduction. Structural basis for nucleotide exchange in heterotrimeric G proteins. Science 348, 1361–1365 (2015). [PubMed: 26089515]
44. Dickson BM, de Waal PW, Ramjan ZH, Xu HE & Rothbart SB A fast, open source implementation of adaptive biasing potentials uncovers a ligand design strategy for the chromatin regulator BRD4. J. Chem. Phys 145, 154113 (2016). [PubMed: 27782467]
45. Huang WJ et al. Structural insights into μ-opioid receptor activation. Nature 524, 315–321 (2015). [PubMed: 26245379]
46. Rose AS et al. Position of transmembrane helix 6 determines receptor G protein coupling specificity. J. Am. Chem. Soc 136, 11244–11247 (2014). [PubMed: 25046433]
47. Caro LN et al. Rapid and facile recombinant expression of bovine rhodopsin in HEK293S GnTI$^-$ cells using a *PiggyBac* inducible system. Methods Enzymol. 556, 307–330 (2015). [PubMed: 25857788]
48. Hornsby M et al. A high through-put platform for recombinant antibodies to folded proteins. Mol. Cell Proteomics 14, 2833–2847 (2015). [PubMed: 26290498]
49. Paduch M & Kossiakoff AA Generating conformation and complex-specific synthetic antibodies. Methods Mol. Biol 1575, 93–119 (2017). [PubMed: 28255876]
50. Scheres SH RELION: implementation of a Bayesian approach to cryo-EM structure determination. J. Struct. Biol 180, 519–530 (2012). [PubMed: 23000701]
51. Brilot AF et al. Beam-induced motion of vitrified specimen on holey carbon film. J. Struct. Biol 177, 630–637 (2012). [PubMed: 22366277]
52. Rohou A & Grigorieff N CTFFIND4: fast and accurate defocus estimation from electron micrographs. J. Struct. Biol 192, 216–221 (2015). [PubMed: 26278980]

53. Pettersen EF et al. UCSF Chimera—a visualization system for exploratory research and analysis. J. Comput. Chem 25, 1605–1612 (2004). [PubMed: 15264254]
54. Emsley P & Cowtan K Coot: model-building tools for molecular graphics. Acta Crystallogr. D 60, 2126–2132 (2004). [PubMed: 15572765]
55. Wang RY et al. Automated structure refinement of macromolecular assemblies from cryo-EM maps using Rosetta. eLife 5, e17219 (2016). [PubMed: 27669148]
56. Adams PD et al. PHENIX: a comprehensive Python-based system for macromolecular structure solution. Acta Crystallogr. D 66, 213–221 (2010). [PubMed: 20124702]
57. Chen VB et al. MolProbity: all-atom structure validation for macromolecular crystallography. Acta Crystallogr. D 66, 12–21 (2010). [PubMed: 20057044]
58. Manglik A et al. Structural insights into the dynamic process of β_2-adrenergic receptor signaling. Cell 161, 1101–1111 (2015). [PubMed: 25981665]
59. Šali A & Blundell TL Comparative protein modelling by satisfaction of spatial restraints. J. Mol. Biol 234, 779–815 (1993). [PubMed: 8254673]
60. Mahalingam M, Martínez-Mayorga K, Brown MF & Vogel R Two protonation switches control rhodopsin activation in membranes. Proc. Natl Acad. Sci. USA 105, 17795–17800 (2008). [PubMed: 18997017]
61. Ranganathan A, Dror RO & Carlsson J Insights into the role of $Asp79^{2.50}$ in β_2 adrenergic receptor activation from molecular dynamics simulations. Biochemistry 53, 7283–7296 (2014). [PubMed: 25347607]
62. Huang J et al. CHARMM36m: an improved force field for folded and intrinsically disordered proteins. Nat. Methods 14, 71–73 (2017). [PubMed: 27819658]
63. Zoete V, Cuendet MA, Grosdidier A & Michielin O SwissParam: a fast force field generation tool for small organic molecules. J. Comput. Chem 32, 2359–2368 (2011). [PubMed: 21541964]
64. Bussi G, Donadio D & Parrinello M Canonical sampling through velocity rescaling. J. Chem. Phys 126, 014101 (2007). [PubMed: 17212484]
65. Dickson BM, de Waal PW, Ramjan ZH, Xu HE & Rothbart SB A fast, open source implementation of adaptive biasing potentials uncovers a ligand design strategy for the chromatin regulator BRD4. J. Chem. Phys 145, 154113 (2016). [PubMed: 27782467]
66. Dickson BM Overfill protection and hyperdynamics in adaptively biased simulations. J. Chem. Theory Comput 13, 5925–5932 (2017). [PubMed: 28974089]
67. Kohlhoff KJ et al. Cloud-based simulations on Google Exacycle reveal ligand modulation of GPCR activation pathways. Nat. Chem 6, 15–21 (2014). [PubMed: 24345941]
68. Alexander SPH et al. The Concise Guide To Pharmacology 2017/18: G protein-coupled receptors. Br. J. Pharmacol 174 (Suppl. 1), S17–S129 (2017). [PubMed: 29055040]

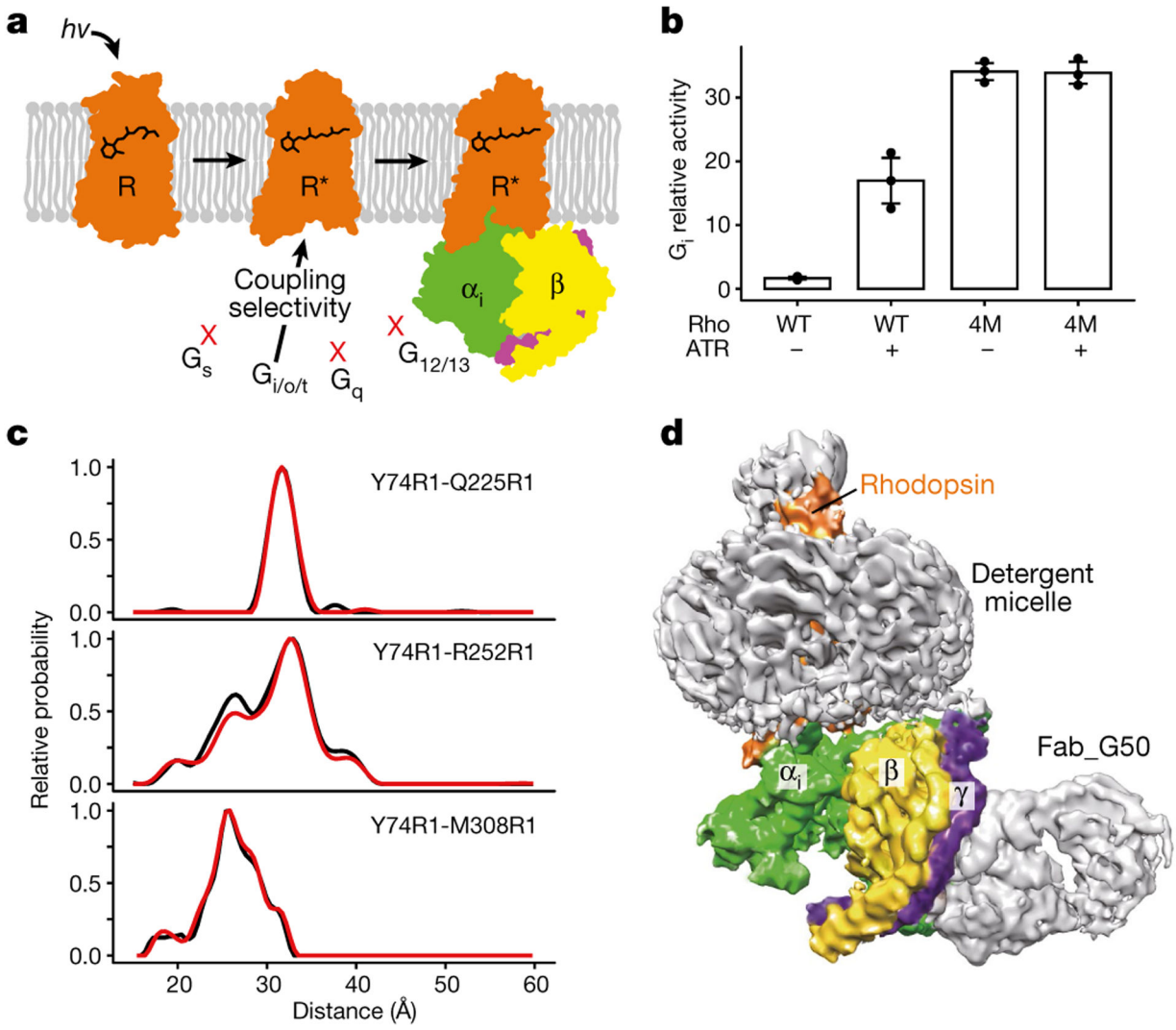

Fig. 1 |. Assembly of the rhodopsin–G_i protein complex.

a, Schematic illustration of G-protein-mediated GPCR signalling by the four types of G protein. Light-activated rhodopsin is specifically coupled to the Gi/o/t subtype. **b**, G_i signalling activated by the 4M mutant and wild-type (WT) rhodopsin as measured by a serum response element (SRE)-driven luciferase reporter assay ($n = 3$). Data are mean ± s.d. **c**, Experimental DEER distance distributions of rhodopsin in the presence (red line) or absence (black line) of Fab. Y74R1-Q225R1, Y74R1-R252R1 and Y74R1-M308R1 denote R1 nitroxide pairs. **d**, Iso-surface rendering of the cryo-EM density map for the rhodopsin–G_i–Fab complex.

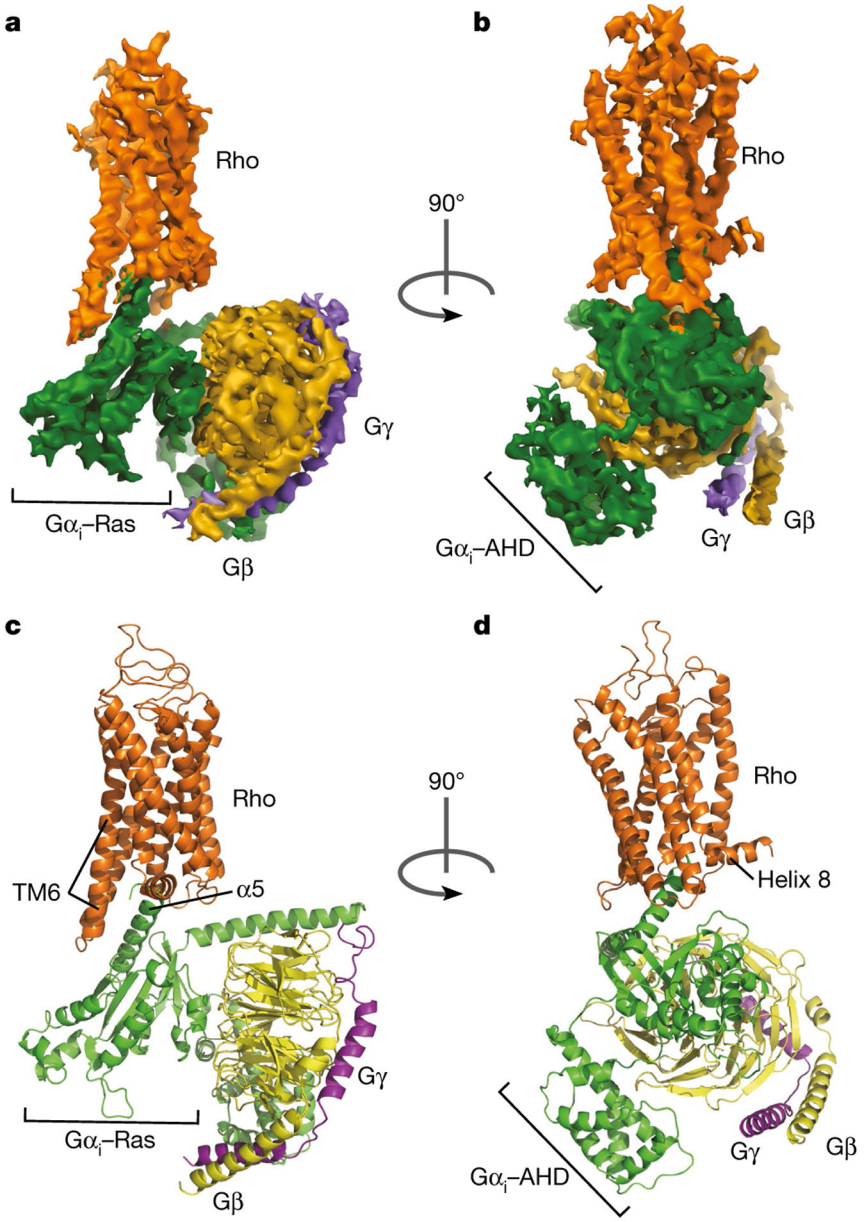

Fig. 2 |. The cryo-EM structure of the rhodopsin–G_i complex.

a, **b**, Orthogonal views of the cryo-EM density map of the rhodopsin–G_i complex, coloured by subunits. **c**, **d**, Ribbon diagram representation of the structure of the rhodopsin–G_i complex.

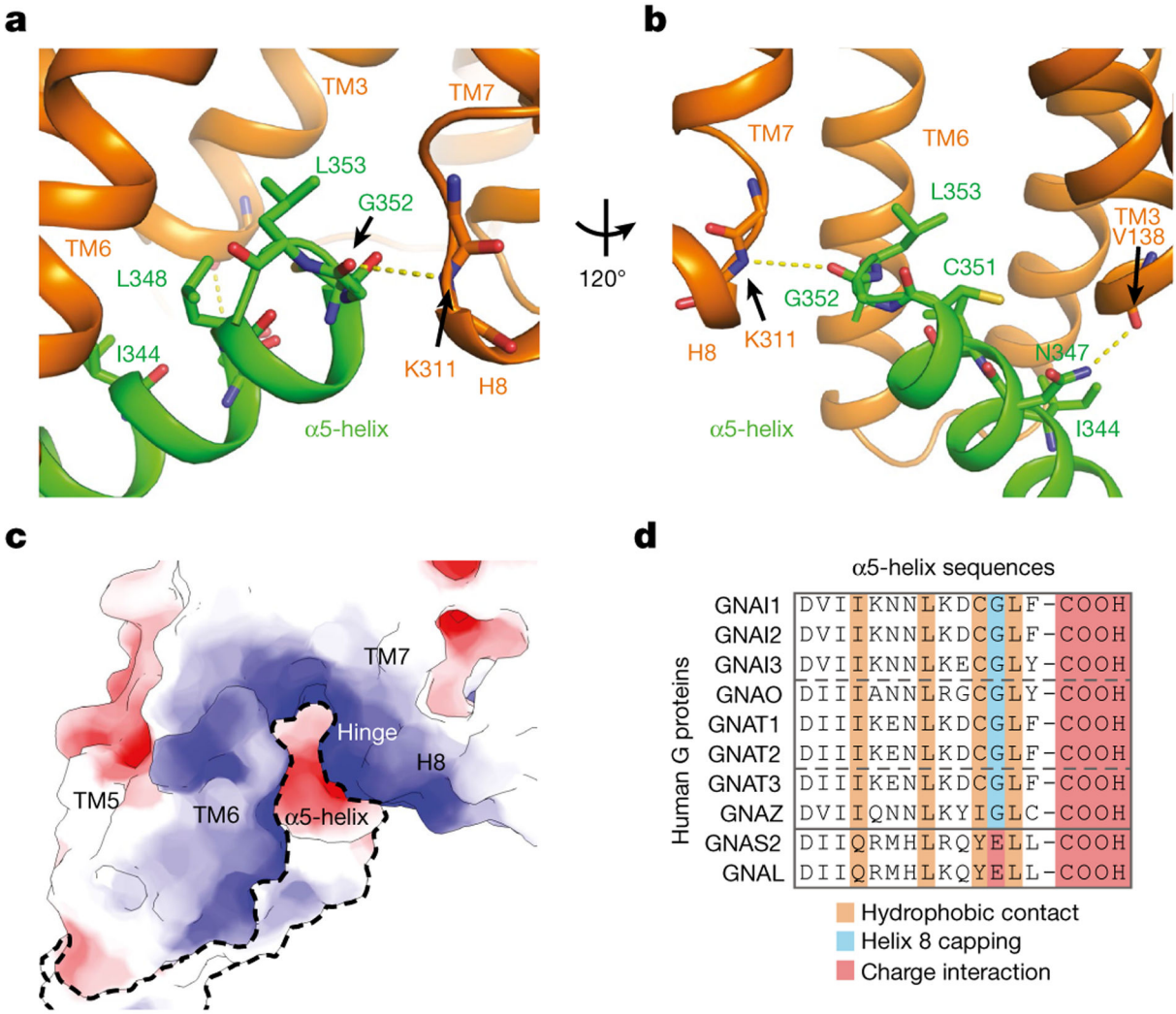

Fig. 3 |. The rhodopsin–G_i interface.

a, **b**, Two views of the binding interface between the α5-helix of the $G\alpha_i$ Ras-like domain and the TMD cavity of rhodopsin. **c**, Rendering of electrostatic surfaces involved in interaction of rhodopsin and $G\alpha_i$, with blue for positively charged regions and red for negatively charged regions. **d**, Sequence alignment of the last 11 residues of the α5-helix from different G proteins, with key residues in receptor binding highlighted by colour shading.

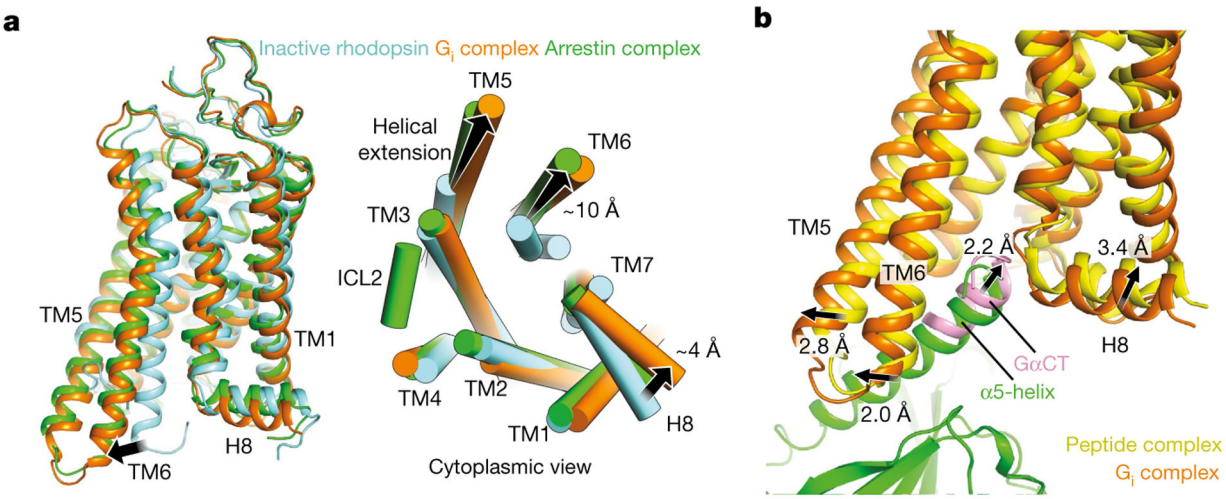

Fig. 4 |. Structural comparison of G_i-bound rhodopsin with inactive rhodopsin, arrestin-bound rhodopsin, and GαCT-bound rhodopsin.

a, Side and cytoplasmic views of the G_i-bound transmembrane bundle (orange) in superposition to the inactive rhodopsin (PDB code 1U19, cyan) and arrestin-bound rhodopsin (PDB code 4ZWJ, green). **b**, Superposition of G_i-bound rhodopsin (orange) with GαCT-bound rhodopsin (yellow). Differences in transmembrane domains at the cytoplasmic faces are highlighted.

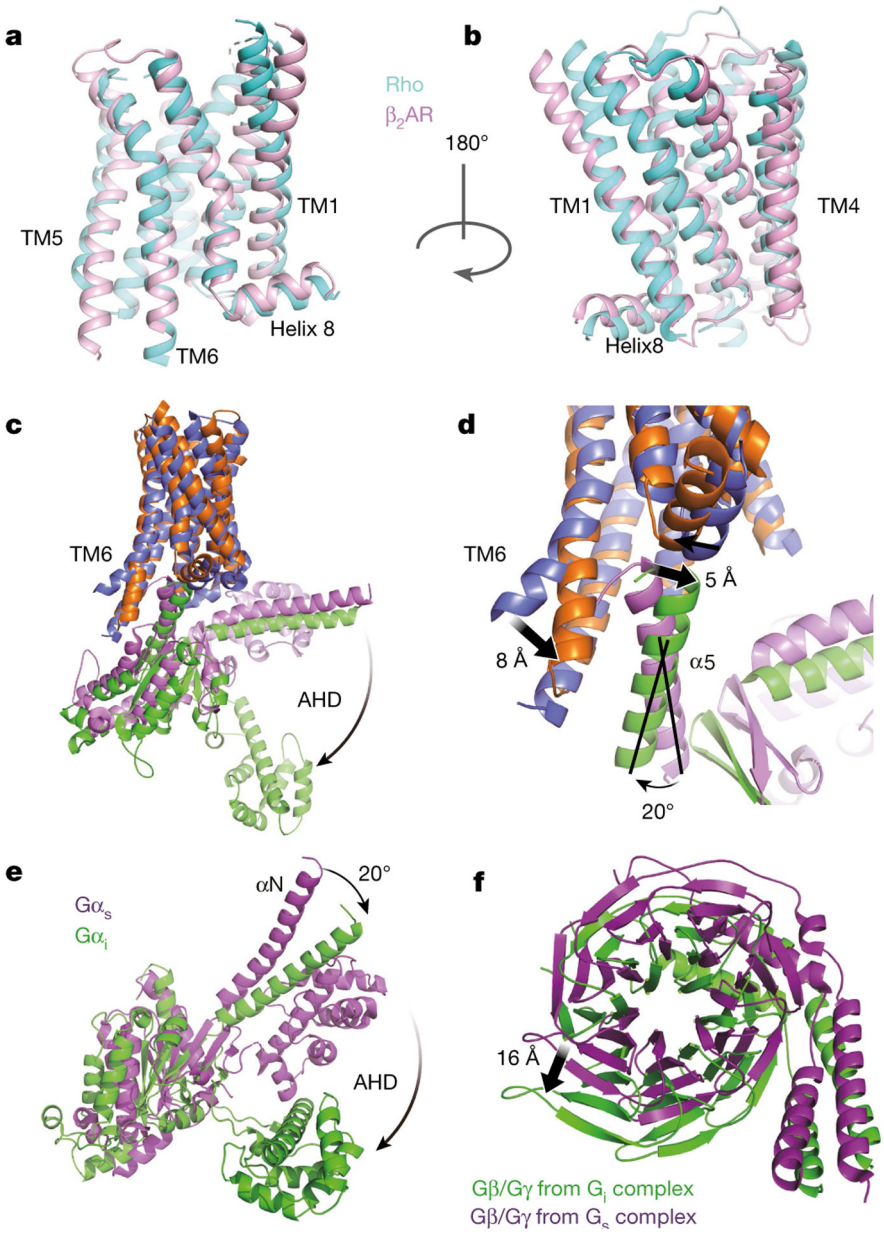

Fig. 5 |. Structural comparison of G_i-bound rhodopsin with G_s-bound β_2AR.

a, **b**, Side view of the inactive rhodopsin structure (PDB code 1U19, cyan) superposed with inactive β_2AR (PDB code 2RH1, pink). **c**, **d**, Side and cytoplasmic views of G_i-bound rhodopsin compared to G_s-bound β_2AR (PDB code 3SN6, blue). Notable structural changes are seen for the intracellular domains of TM6 with a difference of approximately 8 Å at the cytoplasmic end of the helix. The α5 helix of $G\alpha_i$ (green) is rotated 20° away from TM6 compared to that of $G\alpha_s$ (purple). As indicated, there are differences in the locations of the α-helical domains (AHD) of these two G proteins. **e**, **f**, Illustration of the 20° rotation of $G\alpha_i$ (**e**) and the 16 Å shift in βγ as compared to the structure of G_s (**f**).

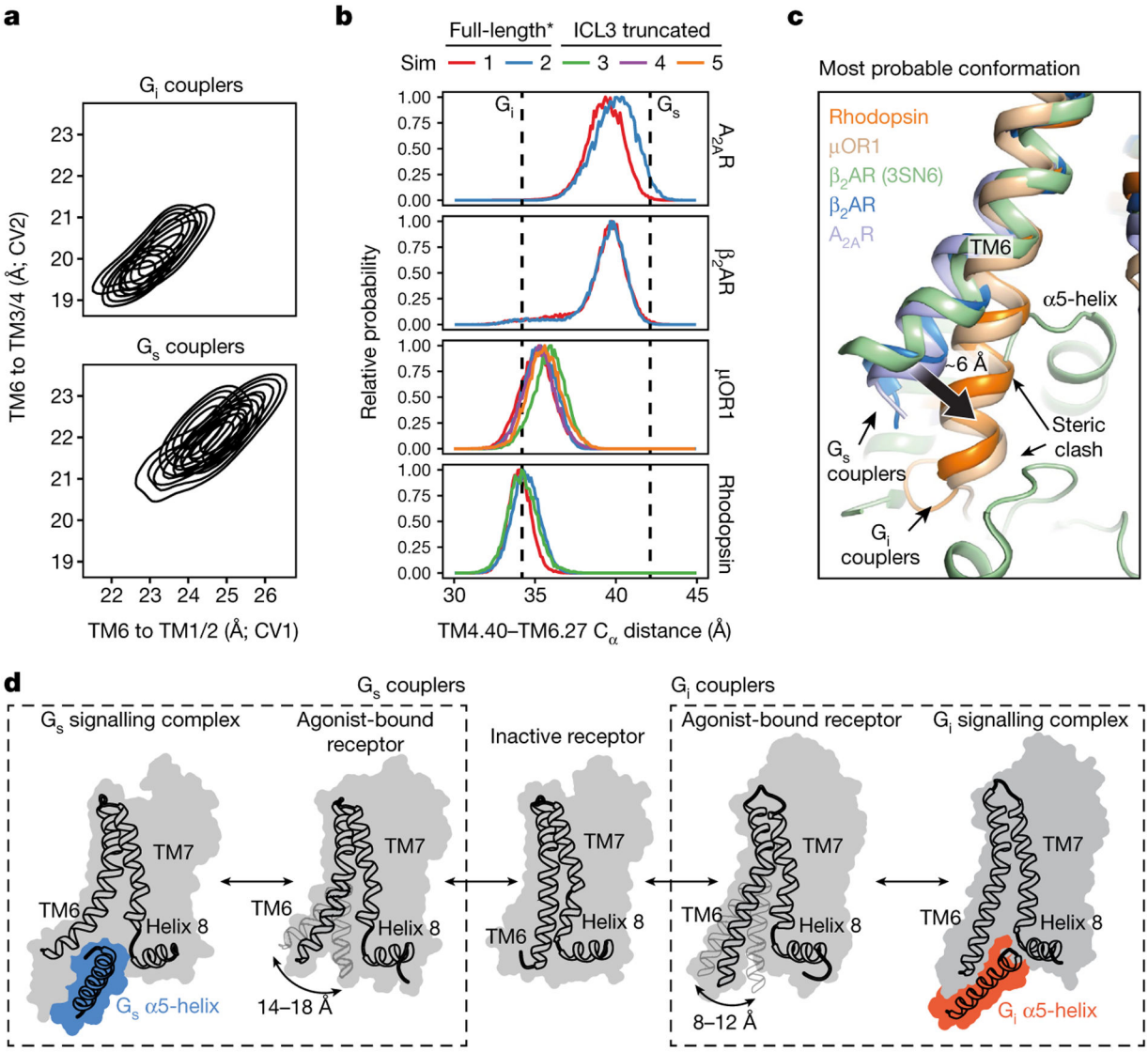

Fig. 6 |. TM6 dynamics of G_i- and G_s-coupled receptors.

a, G_i-coupled receptors exhibit a markedly constrained range of motion compared to G_s-coupled receptors. Comparison of overlapped free energy landscapes truncated at 10 kJ mol $^{-1}$ for G_i- and G_s-coupling GPCRs plotted with their collective variables used for mABP simulations. CV1 and CV2, collective variables 1 and 2, respectively. **b**, Weighted TM4.40 to TM6.27 C_α distance distributions for full-length (simulations 1 and 2) and ICL3-truncated receptor simulations (simulations 3–5). An asterisk on full-length indicates that ICL3 was absent in both G_s couplers. Reference distances for G_i- and G_s-bound states (shown as black vertical dashed lines) are taken from the structure reported here and the β_2AR–G_s protein complex (PDB code 3SN6). For G_i-coupled receptors with and without a complete ICL3, the outward movement of TM6 is approximately 6 Å less than that of G_s couplers. **c**, Representative snapshots of the most probable TM6 position taken from the first simulation replicate, overlapped with the β_2AR–G_s crystal structure. Steric clashed can be seen between the TM6 of both G_i couplers and G_s. **d**, Schematic depicting alternative TM6

conformational states as the structural determinants for selective coupling of G_i and G_s. TM6 distance ranges were calculated using the structure of inactive rhodopsin (PDB code 1F88) as a fixed reference point.